The Internet of Bodies: A Systematic Survey on Propagation Characterization and Channel Modeling

Abdulkadir Celik, *Senior Member, IEEE*, Khaled N. Salama, *Senior Member, IEEE*, and Ahmed M. Eltawil, *Senior Member, IEEE*

***Abstract*—The Internet of Bodies (IoBs) is an imminent extension to the vast Internet of Things domain, where interconnected devices (e.g., worn, implanted, embedded, swallowed, etc.) are located in-on-and-around the human body form a network. Thus, the IoB can enable a myriad of services and applications for a wide range of sectors, including medicine, safety, security, wellness, entertainment, to name but a few. Especially, considering the recent health and economic crisis caused by the novel coronavirus pandemic, also known as COVID-19, the IoB can revolutionize today's public health and safety infrastructure. Nonetheless, reaping the full benefit of IoB is still subject to addressing related risks, concerns, and challenges. Hence, this survey first outlines the IoB requirements and related communication and networking standards. Considering the lossy and heterogeneous dielectric properties of the human body, one of the major technical challenges is characterizing the behavior of the communication links in-on-and-around the human body. Therefore, this article presents a systematic survey of channel modeling issues for various link types of human body communication (HBC) channels below 100 MHz, the narrowband (NB) channels between 400 and 2.5 GHz, and ultrawideband (UWB) channels from 3 to 10 GHz. After explaining bio-electromagnetics attributes of the human body, physical, and numerical body phantoms are presented along with electromagnetic propagation tool models. Then, the first-order and the second-order channel statistics for NB and UWB channels are covered with a special emphasis on body posture, mobility, and antenna effects. For capacitively, galvanically, and magnetically coupled HBC channels, four different channel modeling methods (i.e., analytical, numerical, circuit, and empirical) are investigated, and electrode effects are discussed. Finally, interested readers are provided with open research challenges and potential future research directions.**

***Index Terms*—Body area networks, body channel, capacitive, channel modeling, galvanic, Internet of Things (IoT), intrabody communications (IBCs), narrowband (NB), phantoms, ultrawideband (UWB).**

I. Introduction

THE Internet of Things (IoT) is a technological revolution that integrates the physical and digital worlds by interconnecting uniquely identifiable smart objects [1]. The IoT targets at ubiquitous connectivity among anyone/anything at any place/time for any service over any network. The recent report of international data corporation forecasts that an estimated 22 billion IoT devices in 2018 are foreseen to reach 41.6 billion in 2025, generating 79.4 zettabytes of data.[1] These numbers and ambitious goals naturally propel IoT as a mega-trend in next-generation communication and information technologies (ICTs). As enabler of such a holistic approach towards digitizing and connecting a plethora of devices, all legacy telecommunications, and networking technologies have come under the umbrella of IoT. Therefore, the IoT era dictates a radical paradigm shift in our perception of almost all verticals, including business, industry, energy, media, education, public health and safety, transportation, and logistics. The IoT can be classified into *Internet of X-Things* where *X* may stand for space [2], underground [3], underwater [4], industrial [5], wearable [6], defense and public safety [7], medical [8], and so on. In this survey, we narrow the scope to the body-centric IoT, which will be referred to as the Internet of Bodies (IoBs) throughout the text.

A. Taxonomy of IoB Devices

The IoB is an imminent extension to the vast IoT domain, where connected devices located in-on-and-around the human body form a network to enable a myriad of applications. Although an early version of IoB was first conceptualized in the realm of wireless body area networks (WBANs) [9], their wide-spread use in today's daily life has become possible as a result of parallel advancements in microelectronics, wireless communications, and signal processing. The IoB devices can be worn, swallowed, implanted in the body, or even embedded into the skin. Smartwatches, fitness tracker rings/wrist-bands, wireless headphones, heads-up display glasses, virtual reality headsets, smart tattoos/bio-patches, and global positioning system (GPS) enabled shoes are examples of wearable IoB devices. Digital drug delivery pills and ingestible sensors (e.g., endoscopy capsules) are typical examples of swallowable IoB devices. For implantable IoB, cardioverter defibrillators and heart pacemakers are a case in point. Finally, embedded IoB devices can be simply chips buried under the skin, such as injecting a large rice grain size microchip into the hand for the purpose of biometric identification and authorization grant. All such variety of IoB node types will facilitate a network infrastructure in-on-and-around the human body and eventually pave the way for cutting-edge neurotechnology applications,

Manuscript received October 1, 2020; revised March 3, 2021 and June 19, 2021; accepted July 14, 2021. Date of publication July 19, 2021; date of current version December 23, 2021. *(Corresponding author: Abdulkadir Celik.)*

The authors are with the Computer, Electrical, and Mathematical Sciences and Engineering Division, King Abdullah University of Science and Technology, Thuwal 23955-6900, Saudi Arabia (e-mail: abdulkadir.celik@kaust.edu.sa).

This article has supplementary downloadable material available at https://doi.org/10.1109/JIOT.2021.3098028, provided by the authors.

Digital Object Identifier 10.1109/JIOT.2021.3098028

[1] https://www.idc.com/getdoc.jsp?containerId=prUS45213219

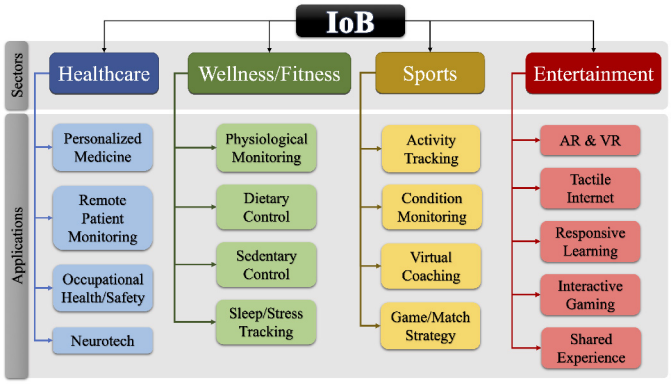

Fig. 1. Taxonomy of IoB applications.

such as brain-computer interface, cognitive assessment and enhancement, neuroinformatic, and neurofeedback [10].

B. Taxonomy of IoB Applications

As pictorially categorized in Fig. 1, IoB devices located in-on-and-around the human body enable many services for a wide range of sectors, each with various applications and functions. Among all these sectors, public health care and safety require specific attention as world population growth poses three major challenges [11]: 1) the demographic peak of baby boomers; 2) the aging population as a result of the increasing life expectancy; and 3) boosting health care expenditures. 2019 base estimates of the Organization for Economic Co-operation and Development (OECD) foresee health spending of member countries to reach 10.2% of gross domestic product (GDP) by 2030, the highest 21.3% for the USA, up from 8.8% in 2015 [12]. These statistics mandate a dramatic shift toward a more scalable and affordable health-care system. More importantly, millions of people die from diabetes, obesity, cancer, cardiovascular diseases, asthma, and many more fatal or chronic diseases every single year. The majority of the current fatal diseases share one critical feature in common: most of the patients have the disease diagnosed a long while after they experience the early symptoms. Research has shown that early diagnosis and screening can control or even prevent most chronic diseases. Therefore, IoB can support future health-care systems for early detection and prevention of diseases through proactive wellness screening technologies. By enabling close and continuous monitoring, IoB can also be an effective tool for the rehabilitation of patients recovering after surgery or medication.

Indeed, all the statistics presented in the previous paragraph have to be reconsidered in the post-COVID-19 world. The COVID-19 is a respiratory virus that originated from the city of Wuhan, China, in December 2019. In March 2020, the World Health Organization (WHO) declared COVID-19 as a global pandemic. The WHO situation reports record almost 25 million infections and nearly a million deaths by September 1, 2020 [13]. In this regard, IoB can be of great help in fighting pandemic diseases by detecting new cases based on physiological data and vital signs, remote monitoring of positive but asymptomatic patients in self-quarantine, and tracing other potential cases in contact with cases previously identified as positive. IoB-based health monitoring is also a good solution to minimize the infection risk for health-care providers whose dedicated-selfless-and-relentless efforts have been proven priceless on the front-line against COVID-19.

C. IoB Risks, Concerns, and Challenges

Albeit, with all these fantastic opportunities, several risks, concerns, and challenges must still be addressed to realize the full potential of IoB. Security risks and privacy concerns are the major obstacles hindering the wide-spread use of IoB devices. This is especially crucial for IoB devices that have control over vital body functions (e.g., heart pacemakers) or gather sensitive data of users. Although laws and regulations exist regarding personal health information held by medical providers and insurance companies, these outdated regulations do not address technology companies that store and process sensitive information in their data centers. Focusing only on the "deemed" sensitivity of certain data items, does not necessarily address the ability to use non-sensitive data to infer sensitive information by means of data analytics.

There are also technical challenges in terms of contradictory design objectives, such as safety, miniaturization, battery life, and communication performance. For example, an implant/embedded IoB device requires both a small form factor and long-battery life. On the other hand, safety regulations limit the maximum transmission power to avoid harm to the human body, which also behaves as a delimiter on communication performance. As a lossy and heterogeneous dielectric medium, the communication channel's characterization in-on-and-around the human body is not only nontrivial but also crucial to optimize overall communication performance. This is mainly because of the fact that the cross-layer optimization of the IoB network heavily depends on precise channel estimation. Noting that subsequent sections go over IoB requirements in detail, the focus of this survey will be on the channel modeling and their interwoven relations with risks, concerns, and challenges.

D. Survey Contributions and Organization

As tabulated in Table I, several magazine and survey papers covered different aspects of WBANs in the last decade.[2] Baldus *et al.* [15] and Cao *et al.* [16] presented a short review of applications, devices, and challenges of WBANs. It is followed by several survey papers which handle WBANs in a layer-by-layer fashion [9], [17], [18], [22], [23]. Since these works cover a wide range of WBAN related issues, they do not provide readers with an in-depth insights into the channel modeling issues. On the other hand, the in-body channel

[2]Table I is generated by searching several scientific databases (e.g., Web of Science, IEEE Xplore, Scopus, Science Direct, etc.) using this article's index terms as keywords. Out of the returned results, we narrowed our focus to the last 15 years and selected papers based on their relevance, content, and widespread referencing as indicated by citations.

TABLE I
RELATED WORKS

Surveys and Magazines on IoB Communications and Networking			
Year	**Ref.**	**Type**	**Content & Style**
2007	[14]	Magazine	Antennas & propagation for on-body WBAN
2009	[15]	Magazine	Principles and challenges of HBCs
2009	[16]	Magazine	A review of WBAN applications, devices, and radio technologies
2011	[17]	Survey	A layer-by-layer survey of WBAN
2011	[9]	Survey	A layer-by-layer survey of WBAN
2012	[18]	Survey	A layer-by-layer survey of WBAN
2013	[19]	Magazine	Propagation models for in-body WBAN
2013	[20]	Magazine	Propagation models for on-body WBAN
2013	[21]	Survey	A survey on intrabody communications
2014	[22]	Survey	A layer-by-layer survey of WBAN
2014	[23]	Survey	A survey on technologies & design challenges
2017	[24]	Survey	A review on HBC
2018	[25]	Survey	A survey of galvanic coupling HBC

characterization is reviewed in [19], which is followed by on-body channel characterization in [14] and [20]. The surveys on human body communication (HBC) is relatively more recent and can be found in [24] and [25].

In previous surveys, channel characteristics were either briefly mentioned or considered for a specific type of channel (e.g., in-body or on-body). To the best of the authors' knowledge, this survey is the first to provide a systematic survey on modeling narrowband (NB), ultrawideband (UWB), and HBC channels in-on-and-around the human body. We call it a systematic survey for two reasons: 1) it systematically organizes channel models based on frequency band, node locations, and combinations of various link types. These are investigated from first and second-order channel statistics (SOCs) perspectives, which are further classified based on their impact scale, i.e., small or large and 2) the survey is not only intended for presenting state-of-the-art channel modeling and propagation characterization studies. Throughout the survey, we discuss how the channel model accuracy is coupled with IoB communication systems and networks' design. We are also the first to present the IoB concept as a holistic view and system-level requirements and related standards. Fig. 2 presents the survey organization along with the number of references falls within each section and/or section. Fig. 2 also shows a time-span of research topics to illustrate the phases of propagation characterization and channel modeling studies and the related standardization efforts.

II. IOB REQUIREMENTS AND RELATED STANDARDS

Standardizing the IoB communications and networking is a challenging task due to the broad range of IoB applications presented in Section I-B. The standardizations bring many benefits, including reduced research and development costs thanks to the publicly available solid technical specifications and guidelines; compatibility and interoperability between products manufactured by different vendors; rapid and broad spread of the technology. Therefore, this section first outlines the main IoB requirements before delving into the various entities' standardization efforts.

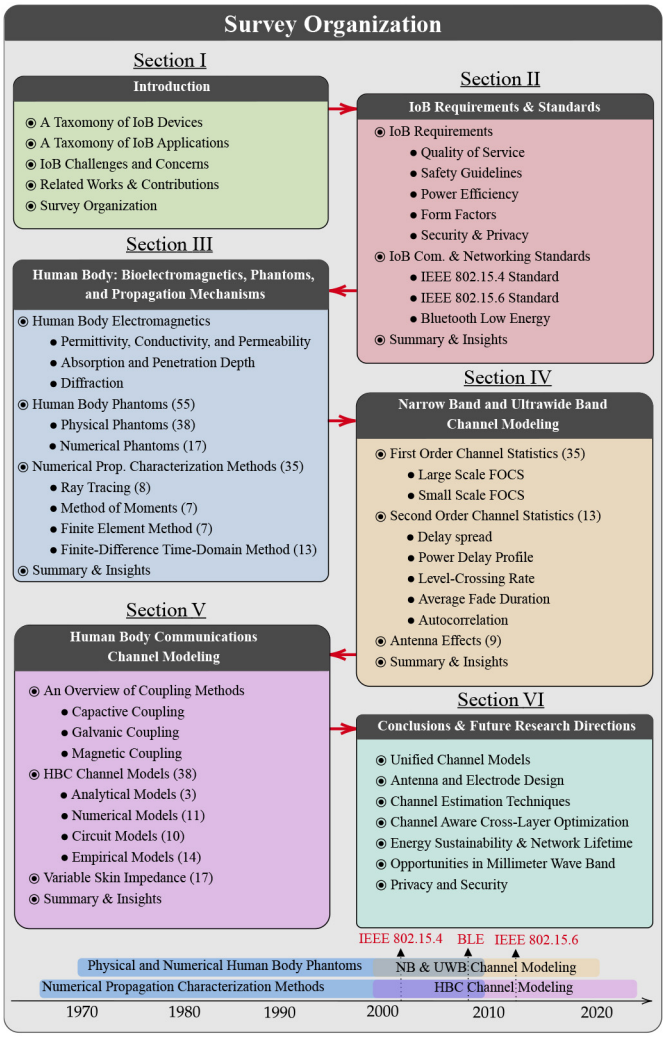

Fig. 2. Schematic illustration of the survey organization.

A. IoB Requirements

In this section, we briefly summarize the main IoB requirements in light of the application types discussed above.

1) Quality of Service: The Quality of Service (QoS) demands of IoB applications can significantly deviate from each other in terms of data rate, bit error rate (BER), latency, and reliability. The data rate needs may range from Kbps (e.g., glucose monitoring: $<$ 1 Kb/s, drug delivery: $<$ 16 Kb/s, EEG: 86.4 Kb/s, voice: 50–100 Kb/s, ECG: 192 Kb/s) to Mb/s (e.g., capsule endoscopy and audio streaming: 1 Mb/s, EMG: 1.5 Mb/s, video streaming: 10–100 Mb/s) [23]. While medical and military applications have stringent BER demands ($< 10^{-10}$), multimedia applications are relatively more tolerable ($< 10^{-5}$). Since medical and military applications generally fall within the scope of ultrareliable low-latency communications (URLLCs) class, IoB network architecture should be designed to provide a diverse range of QoS demands by prioritizing traffic types based on urgency and criticality of the underlying applications.

At this point, the coexistence of IoB nodes and other wireless technologies has significant impacts on meeting the QoS demands. Generic IoT devices are generally designed to

operate on license-free globally available industrial-scientific-and-medical (ISM) bands, which are already overcrowded by other wireless standards, including IEEE 802.11 (Wi-Fi) [26], IEEE 802.15.1 (WPAN) [27], IEEE 802.15.4 (ZigBee) [28], and Bluetooth [29]. The coexistence of IoBs and these standards are addressed in [30]–[32]. Considering the ever-increasing IoT devices operating on ISM bands, it is hardly possible to guarantee URLLC for critical IoB applications. Therefore, the physical layer (PHY) should employ appropriate interference avoidance and error correction methods to improve BER performance. Moreover, the PHY should also be supported by higher layers to improve packet loss rate and transmission delays with effective collision and congestion avoidance techniques.

2) Safety Guidelines: In the context of wireless communications, the primary health concern is mainly heating of body tissues since the energy of transmitted electromagnetic (EM) fields is absorbed by the body. The degree of heating effects due to the overexposure to EM fields depends on the operating frequency, signal intensity, the duration of exposure, the location of exposure on the human body, the distance from the transmitter as well as other factors such as shielding. General safety guidelines are specified by the International Commission on Non-Ionizing Radiation Protection (ICNIRP) to limit time-varying EM field exposure on the human body [33]. For frequencies up to 10 GHz, these restrictions are determined in terms of specific absorption rate (SAR), which is expressed in units of watts per kilogram [W/Kg]. Thus, the SAR represents the mass normalized energy rate coupled to biological tissues. Indeed, typical low-power wireless devices do not radiate enough power to be a concern for whole-body SAR. However, since IoB devices are located in or on the human body, extra attention must be paid on localized SAR measured around the transceivers in/on the human body. Therefore, IoB related standards must comply with the minimum local SAR requirements of global (ICNRP [33]) or regional regulation entities, e.g., scientific committee on emerging and newly identified health risks (SCENIHRs) for European Union [34] and Federal Commission on Communications (FCCs) for USA [35].

3) Power Efficiency: IoB nodes are specially designed as ultralow-power communication devices for two main reasons: 1) to comply with the safety regulations mentioned above and 2) to maximize the network lifetime since IoB devices are typically battery powered. In particular, implanted and embedded IoB nodes require five years of battery lifetime as they are typically placed in the human body through a surgery process [36]. Likewise, wearable devices and on-body sensors are also preferred to have a lifetime of weeks or months for the sake of user satisfaction and maintenance easiness. A cross-layer optimization is necessary for an energy-efficient system design, which is discussed in the subsequent sections of the survey.

4) Form Factor: IoB nodes generally have stringent form factor constraints that require squeezing antenna/electrode and battery into a tiny case while meeting the QoS demands of the application of interest. While miniaturization is crucial for implantable devices, flexibility, and stretchability are more important comfort considerations for wearable devices [37]. Advances in stretchable electronics is a key technology to realize flexible wearable devices; e.g., liquid and microfluidic antennas, displays, solar cells, battery, sensors, etc. Ink-jet printable textile electronics can also realize highly effective small form-factor wearable devices [38]. Notice that antenna/electrode design for on/in-body devices is quite distinct due to the impacts of the human body on the radiation and polarization characteristics, which is discussed in more detail through Sections IV-C and V-C.

5) Security, Confidentiality, and Privacy: Most IoB applications require a high level of security, confidentiality, and privacy. However, this is a challenging task given the limited resources of energy, memory, and computational power. First of all, a trusted coordinator node is necessary for the management of adding/dropping nodes to/from the network as well as providing key distribution for encryption and decryption. The coordinator and IoB nodes also need to authenticate that data is received from a trusted pair, which can be done by computing a message authentication code based on a shared secret key. The integrity of data should also be protected against the adversary nodes' capabilities of altering original data. Furthermore, the confidentiality of user data must be carefully guarded against eavesdropping. Data integrity and privacy are especially important if the underlying application is sensitive to the age of information (e.g., data freshness). Since ensuring all these functions inevitably degrades other QoS metrics, the use of biometrics can help significantly reduce the complexity and its associated costs [39], [40]. The biometrics include heartbeat timing, fingerprint, voice, palm print and veins, face/iris recognition, gait, typing rhythm, etc. Unlike the license-free crowded RF bands, HBCs offer extra levels of physical layer security by using the human body as a communication medium, which is also discussed in the subsequent sections of the survey.

B. IoB-Related Communications and Networking Standards

In this section, we summarize the main features of IEEE 802.15.4, IEEE 802.15.6, and Bluetooth standards. Although they are developed for WBANs, we believe they provide a good starting point for standardization of the IoB networks.

1) IEEE 802.15.4 Standard: The IEEE 802.15.4 standardizes the PHY and MAC specifications to support low cost, low power, low range, and low bit rate requirements of wireless personal area networks (WPANs) [28]. The upper layer operations of The IEEE 802.15.4 are defined by the ZigBee protocol of ZigBee Alliance [41] and 6LowPAN of the Internet engineering task force (IETF) [42]. The ZigBee protocol suite is later extended to ZigBee Pro for nonrouting nodes with extra features of route aggregation, asymmetric link handling, conflict resolution, etc.

The IEEE 802.15.4 specifies a total of 27 half-duplex channels: a single channel with 20 Kb/s rate at 868-MHz band, ten channels each with 40 Kb/s at 915-MHz band, and 16 channels each with 250 Kb/s at 2.45-GHz band. In the MAC layer, beacon-enabled and nonbeacon-enabled channel access modes are available. While the former employs the

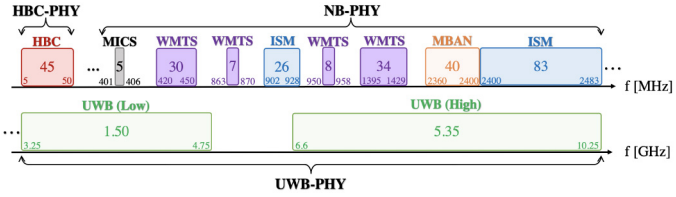

Fig. 3. Frequency bands defined by IEEE 802.15.6 Standard.

carrier sense multiple access/collision avoidance (CSMA/CA) algorithm with back-off periods, the later uses an unslotted CSMA/CA. Although an encryption algorithm is defined to cipher the transmitted data, key management and authentication policies are not specified. However, ZigBee manages these issues in the network and application layers by using the advanced encryption standard (AES) with 128-bit key lengths.

2) IEEE 802.15.6 Standard: Unlike the IEEE 802.15.4 standard, the IEEE 802.15.6 standard is especially developed to meet the aforementioned distinctive QoS demands of WBANs [43]. As illustrated in Fig. 3, the IEEE 802.15.6 standard defines three different PHYs to address the breadth of WBAN applications.

1) HBC-PHY operates with a central frequency at 21 MHz and a bandwidth of 5.25 MHz, which may support data rates ranging from 164 Kb/s to 1.3 Mb/s.
2) NB-PHY requires NB-WBAN nodes to operate in at least one of the following bands: medical implant communication service (MICS) band on 402–405 MHz; wireless medical telemetry system (WMTS) bands on 420–450, 863–870, 950–958, and 1395–1429 MHz; medical body area network (MBAN) band on 2360–2400 MHz; and ISM bands on 902–908 and 2400–2483.5 MHz. NB-PHY allows several bit rates ranging from 50 Kb/s to 1 Mb/s by using the Bose–Chaudhuri–Hocquenghem (BCH) error correction codes with basic modulation schemes. For example, Gaussian minimum shift keying (GMSK), $\pi/2$-shifted differential binary phase-shift keying (DBPSK), and $\pi/4$-shifted differential quadrature phase-shift keying (DQPSK).
3) UWB-PHY consists of low (3.25–4.75 GHz) and high (6.60–10.25 GHz) bands, each of which is further divided into 500 MHz sub-bands. The UWB technique is known with its ability to support either low rates over highly attenuated channels or high rates over short ranges. In addition to power-spectral density, its fine granularity time resolution is suitable for real-time applications [44]. The UWB-PHY provides high data rates (0.2–15 Mb/s) by using simple modulation schemes of impulse radio (IR-UWB) and frequency modulation (FM-UWB) with noncoherent detection or differentially coherent detection.

All PHY solutions share a single MAC protocol that has three modes of operation: 1) beacon mode with beacon periods (i.e., superframes); 2) nonBeacon mode with superframes; and 3) nonbeacon mode without superframes. Superframes consist of three phases: 1) exclusive access phase for transmission of critical/emergency data; 2) random-access phase for nodes using CSMA/CA; and 3) contention access phase for nodes using slotted ALOHA access. The IEEE 802.15.6 also supports three levels of security: Level-0) unsecured communications; Level-1) authenticated but not encrypted communications; and Level-2) authenticated and encrypted communications for confidentiality and privacy.

Other requirements of the IEEE 802.15.6 can be summarized as follows: transmission range upper-bound and lower-bound are set as 3 m for in-body and on-body communications, respectively. For 95% of the best-performing links, the packet error rate should be no more than 10% for a 250 octet payload. Nodes should be able to join and leave the network in less than 3 s. Less than 125 and 250 ms latency should be provided for medical and nonmedical applications, respectively. The minimum (maximum) transmission power must be no more (less) than -10 (0) dBm.[3] Finally, up to ten nodes could co-exist in a 6 m^3 space.

3) Bluetooth Low Energy: Bluetooth is a whole protocol stack with two modes of operation: 1) basic rate (BR) and 2) low energy (LE) [29]. The BR is the classic Bluetooth that can provide up to 3 Mb/s with optional enhanced data rate (EHR). LE is especially developed for low-power low-rate cheap devices powered by button cell batteries. Bluetooth operates on 2.45-GHz ISM band which is split into 2 MHz-wide 40 sub-bands. Bluetooth can provide up to 1 Mb/s by using the Gaussian frequency-shift keying (GFSK) modulation. It also has two security modes: 1) the former ensures data integrity and 2) encryption with or without authentication while the latter do not provide encryption. Authentication and encryption are implemented by AES with 128-bit key length and chaining message authentication codes, respectively. Bluetooth also supports privacy by allowing devices to use random addresses over the time, which can be revealed only with a proper key.

C. Summary and Insights

Based on the broad range of IoB applications, this section first presented requirements for QoS, safety, power efficiency, form-factor, security, confidentiality, and privacy. As a result of the conflicting objectives, there are inextricably interwoven relations among these requirements. For example, provisioning a high-QoS demand (e.g., URLLC) requires sophisticated signal processing techniques and advanced communication modules. Resulting computation and hardware complexity inherently conflict with power efficient and small form factor design. Likewise, security and privacy measures have a direct impact on overall system design and network architecture due to its limitations of the QoS performance. Therefore, future IoB standards should sufficiently address these main requirements.

In this regard, we presented three main BAN standards as an initial point for communication and networking standard of the IoB: 1) IEEE 802.15.4; 2) IEEE 802.15.6; and 3) Bluetooth LE. The IEEE 802.15.4 standard (i.e., ZigBee) is developed for generic low-cost low-power WPANs operating on ISM bands.

[3]This complies with FCC's SAR specification of 1.6 W/kg in 1 g body tissue.

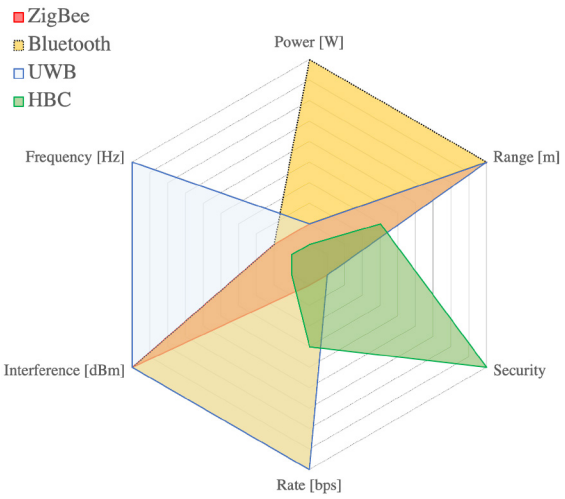

Fig. 4. Qualitative comparison of WBAN technologies.

However, it has been recognized as insufficient to address specifics of body area communications and to support stringent requirements of BAN applications. Similarly, Bluetooth was developed as a whole protocol stack operating also on ISM bands. Considering the ever-increasing number of IoT devices, ZigBee, and Bluetooth suffer from high interference, co-existence issues, security threats, and being limited to on-body communication links. Although communication modules of almost all communication devices are capable of operating on ISM bands, these standards do not offer a complete solution due to their deficiency and vulnerability in supporting the wide range of IoB applications and their requirements. Alternatively, IEEE 802.15.6 is dedicated to BANs with three different PHY options: 1) NB (MICS, WMTS, ISM, and MBAN); 2) UWB; and 3) HBC. To provide readers with a better insight into these communication bands, we present a qualitative comparison of different technologies in Fig. 4. These wide varieties of spectrum ranges pave the way for a better system design tailored to the specific needs of IoB applications because communication channels in-on-and-around the human body have significantly distinctive behaviors at different spectrum bands. In what follows, we delve into reasons behind these behavioral changes based on the EM properties of the human body.

III. Human Body: Phantoms and Propagation Mechanisms

In this section, we first discuss the dielectric properties of the human body, which are of utmost importance to understand the propagation characteristics and improve the accuracy of both analytical and numerical methods. Instead of human and animal experimentation, dielectric data can be helpful to create body phantoms to mitigate cost, complexity, and ethical constraints. Second, we introduce a review of physical and numerical body phantoms. The third section presents EM computational tools that simulate EM propagation based on the numerical body phantoms. We refer interested readers to supplementary materials where we provide fundamental insights into the electromagnetic properties and behaviors of the human body. In this way, electromagnetic propagation characteristics in-on-and-around the human body can be understood more precisely.

TABLE II
Comparison of the Physical HBPs

	Cost	Complexity	Durability	Reusable/Adjustable	Frequency	Accuracy
Liquid	Low	Low	Short-Term	Yes/Yes	400 MHz-2 GHz	Low-Medium
Semiliquid	Low	Low	Short-Term	Yes/Yes	7-868 MHz	Low-Medium
Semisolid	Medium	Medium	Medium-Term	No/No	0.2-10 GHz	Medium-High
Solid	High	High	Long-Term	No/No	1 MHz-10 GHz	Medium-High

A. Human Body Phantoms

To validate the safety and evaluate the performance of IoB devices, their EM interaction with the human body must go through a quantitative and precise investigation in all the possible operation scenarios. However, regulatory bodies require experimental studies on human subjects and human-related materials to receive ethical clearance, which has strict constraints on scientific, physical, and psychological risk levels. To this end, body phantoms mimic dielectric properties of the human body by either numerical or physical models. Thus, body phantoms are useful to system modeling and optimization before human clinical trials. In addition to medical purposes (e.g., X-Ray, hyperthermia, magnetic resonance imaging (MRI), diagnosis, and treatment), body phantoms are also used for SAR measurements, EM dosimetry, implantable, and wearable devices. The human body phantoms (HBPs) can be classified into physical and numerical for the experimental and computational type of research, respectively. We provide a taxonomy of physical and numerical HBPs types in the sequel.

1) Physical HBPs: Based on the chemical compound ingredients, the physical HBPs are categorized into liquid, semiliquid, semisolid, and solid; which can be further categorized based on body parts (e.g., head, torso, limb, breast, etc.) or tissue types (e.g., low and high water content). Before delving into the details, we refer interested readers to Table II for comparison among different physical HBPs.

a) Liquid HBPs: Liquid HBPs are the first and oldest phantom type that is especially suitable for high water content tissues with high-dielectric properties. Therefore, water is the main ingredient whose permittivity and conductivity is adjusted to different tissue types by adding various solvable (e.g., sugar and salt) or dis-solvable (e.g., flour and oil) liquid mixtures. The fabrication procedure of several liquid phantoms is discussed in [82]. The prepared formulas are generally poured into thin containers with low dielectric properties. Depending on the application, the container may have a shape of regular prisms, body parts, or the whole body.

The liquid HBPs have the virtues of low cost and complexity fabrication and suitability for place/replace the measurement probes/sensors. Liquid materials are reusable and adjustable to confine to different dielectric properties by adding extra ingredients. However, they have short-term durability because of the dehydration and mold growth [82]. Moreover, they are limited by frequency ranges up to 6 GHz [90]. Due to the suspension of insoluble ingredients, the formula is required to be stirred, which may result in minor changes in the electrical properties [91]. Finally, the liquid HBPs may have inaccurate

SAR measurements for two reasons [92]: 1) dielectric properties of the container are different from that of liquid and 2) homogeneity of liquid formula limits the accurate modeling of tissue heterogeneity. Khorshid *et al.* [93], [94] were the first to develop a multilayer arm phantom for the five basic tissue layers: 1) skin; 2) fat; 3) muscle; 4) cortical bone; and 5) bone marrow. The model's high accuracy and perfect match are validated by experiments on real subjects.

b) Semiliquid and semisolid HBPs: Semiliquid (gel) and semisolid (jelly) phantoms are fabricated from coagulant materials [95]. Unlike the liquid materials, the semiliquids do not suffer from suspension and sustain the homogeneity for a longer duration. Noting that the semiliquid share the rest of liquid phantoms' virtues and drawbacks, their fabrication takes a relatively long time as slow and continuous rotation is necessary to prevent trapping air bubbles [96].

Unlike the liquid and semiliquid HBPs, the semisolid materials can independently conform to any shape, which eliminates the need for an outer shell. Moreover, their non-diffusive and castable nature allows a multilayered fabrication to mimic the anatomical structure of the human body more realistically. The fabrication procedure of semisolid materials is outlined in [68]. The semisolid HBPs have the virtues of medium-complexity and medium-cost fabrication. Even though the majority of the semisolid HBPs presented an accurate and stable nature for a wide frequency range up to 11 GHz [90], their accuracy is also studied at 55–65 GHz mm-Wave bands [87], [97]. However, they have medium-term durability because of the dehydration and mold growth [68]. Moreover, replacing the measurement probes and sensors may cause the deformation of the phantom shape. Unlike the liquid and semiliquid HBPs, they are neither reusable nor adjustable.

c) Solid HBPs: Solid HBPs can be manufactured from a mixture of the wide variety of materials. The fabrication procedure of solid phantoms can be found in [60]. They can preserve their dielectric properties for an extended period of time since they are not subject to dehydration. However, their fabrication has high-complexity processes involving extreme pressures and temperatures. The complexity and the need for expensive raw materials increase the overall cost. Moreover, they are limited by frequency ranges up to 6 GHz [90]. Similar to the semisolid HBPs, they are neither reusable nor adjustable, and it is not possible to replace the measurement probes and sensors. We refer interested readers to Table III for a list of references categorized based on body parts.

2) Numerical HBPs: Thanks to the ever-increasing computational power, numerical simulations are powerful tools to analyze the radio propagation characteristics of the human body. Numerical HBPs are based on a digital representation of the human body anatomy, which is generally obtained by MRI and computed tomography (CT). MRI and CT provide gray-scale images of resolutions in the order of millimeters, which then goes through coloring and segmentation processes to interpret different colors into various tissue types. In this way, each segment is associated with the corresponding permittivity and conductivity values to solve Maxwell equations [45]. Noting that segmentation is cumbersome and time consuming, an alternative approach is using anthropomorphic numerical models, which are also referred to as dielectric analytical models. These models semi-automatically correlate the gray-scale images to the complex permittivity values by means of continuous transfer functions [98]. Numerical HBPs are categorized into homogeneous and heterogeneous models depending on the homogeneity of the tissue and phantom of interest. We refer interested readers to Table IV for a list of numerical HBPs discussed below.

TABLE III
CATEGORIZATION OF PHYSICAL HBPS

	Body Part	Ref.	Frequency	P/T (F)	Structure	Tissues
PHYSICAL PHANTOMS	Head	[51]	402 MHz	P (L, HO)	ANM, CU	s
		[52]	400 MHz	P (L)	ANM	g
		[53]	835-925 MHz	T (S, HO)	-	m, br, sk
		[54]	0.9 GHz	P (L, HO)	ANM	t liquid (equiv.)
		[55]	0.9 GHz	P (L, ML)	ANM, RE	bo, br, e, g, m, s, w
		[56]	0.9 GHz	P (L, HO)	ST	br liquid (equiv.)
		[57]	7 MHz	P(SL, HO)	ANM	br
		[58]–[60]	(0.9, 1.5) GHz	P (S, HO)	ANM	head equiv.
		[61]	(0.9, 1.75, 1.95) GHz	P (L, HO)	ANM	t (head equiv.)
		[62]	(0.9, 1.8) GHz	P (L, HO)	ANM	head liquid (equiv.)
		[62]	0.9-2 GHz	P (L, HO)	ANM	t (equiv.)
		[63]	2.4 GHz	P (S, HE)	ST	bo, g, m, s, w
		[64]	2.45 GHz	P (S, HE)	BO	bo, s, g, m
		[65]	1 MHz - 10 GHz	P (S, ML)	L, SP	g, f, m
		[66]	0.2-3 GHz	P (SS, ML)	CU, SP	br, sk
		[67], [68]	0.5-4 GHz	P (SS, HE)	MRI	b, e, g, w
		[69]–[72]	1-4 GHz	P (SS, HE)	ANM	g, h, sc, sk, w
		[73], [74]	2-5 GHz	P (SS, ML)	ST	s, bo, g, w
		[75]	3-6 GHz	T (SS, HO)	BO	t
	Torso	[55]	0.9 GHz	P (L, HO)	ANM, RE	br, bo, m, sk
		[76]	868 MHz	P (SL, ML)	Assumed	f, m, sk
		[77], [78]	2.45 GHz	P (L, HO)	BO	m
		[79]	2.45 GHz	T (L, HO)	-	f, m
		[80]	(8.5, 10) GHz	T (SL, HE)	-	bo, f, m
		[81]	<30 MHz	T (SL)	-	m
		[82]	5-40 MHz	T (SS)	-	t (various)
		[83]	0.1-1 GHz	T (L, S, HO)	-	bo, br, l, m
		[84]	0.9-3 GHz	T (L, HO)	-	avg. torso prop.
		[85]	0.9-10 GHz	T (SS, HO)	ST	m
	Limb	[86]	3-6 GHz	T (SS, HO)	-	body and head
		[87]	80-500 MHz	P (SS, HE)	ANM	bo, f, m, tu
		[88]	0.6-6 GHz	P (S, HO)	ANM	hand (b, f, m, te, s)
		[76]	0.9 GHz	P (S, HO)	ANM	t (various)
		[?], [88]	55-65 GHz	P (SS, HO)	ANM	s
		[89]	57-64 GHz	P (SS, HO)	RE	s
LEGEND	P/T (F)	P: Phantom, T:Tissue, HO: Homogeneous, HE: Heterogeneous, ML: Multilayered				
	Materials	L : Liquid, SL: Semiliquid, S: Solid, SS: Semisolid				
	Structure	ANM: Anthropomorphic, CU: Cubic, CY: Cylindrical, HM: Hemispherical, RE: Realistic, ST: Stylized, BO: Box shaped, L: Layered, SP: Spherical				
	Tissues	bl:blood, bo: bone, br: brain, e: eye, f: fat, gl: gland, g: gray-matter, l: lung, m: muscle, s: skin, sc: scalp, sk: skull, w: white-matter, te:tendon, tu:tumor				

a) Homogeneous HBPs: The homogeneous HBPs are generally in the form of simple geometric shapes, such as cylinders, spheres, parallelepipeds, etc. They are generally used to evaluate EM dosimetry applications where the EM field is radiated from simple sources [92]. While spherical phantoms are mainly used for dosimetry inside the human head [99]–[102], cylindrical models are used for whole-body models [103], [104]. A 200-mm^3 cube and a 200-mm diameter sphere models are also proposed in [105]. The Homogeneous HBPs are also used for the confirmation of the validity of numerical tools covered in the next section.

b) Heterogeneous HBPs: The heterogeneous HBPs are also known as volumetric or voxel phantoms as they consist of volumetric cells, i.e., voxels. Their accuracy increases with the number of voxels at the expense of more computation and time complexity. Since the human body exhibits different dielectric properties of different ages and genders, some models provide a set of male and female HBPs at various ages, such as virtual family [106], virtual population 3.0 [107], and GSF family [108]. There are also phantoms dedicated to different nations, such as the Visible Human Model of U.S. National Library of Medicine [109], Japanese male and female model [110], and Chinese adult model [111].

TABLE IV
CLASSIFICATION OF NUMERICAL HBPS

Type	References	Model/Shape	Gender	Age	Resolution (mm)
Homogen.	[51], [55], [59]	Cylindrical Arm Model	-	0-90	-
	[99]	Spherical phantom	-	-	-
	[100]–[102]	Multilayered sphere model of the human skull	-	-	-
	[103]	Cylindrical model for whole body	-	-	-
	[104]	Three-layered elliptical model of the human body	-	-	-
Heterogeneous	[106], [107]	Virtual population	All	5-84	Head: 0.5 x 0.5 x 1.0 Torso + Limb: 0.9 x 0.9 x 2.0
			F, A	26	Body: 2 Implant: 0.5
	[106], [107]	Virtual Family	F, M, A M, F, C	26-34 6-11	Head: 0.5 x 0.5 x 1.0 Torso + Limb: 0.9 x 0.9 x 2.0
	[98]	Dielectric anatomical model	M, A	34	2 x 2 x 2
	[108]	GSF family	F, M, A	38-40	-
			C	2, 7	-
	[109]	Visible human model	-	-	-
	[110]	Japanese Avg. Male and Female	F, M, A	22	2 x 2 x 2
	[111]	Chinese Visible Human project	F, M, A	22-35	1 x 1 x 1

Legend | M: Male, F: Female, A: Adult, C: Children

B. Numerical Propagation Characterization Methods

Apart from dosimetry applications and SAR measurements, numerical modeling of RF propagation has distinct features since the human body acts as a transmission medium and/or reflectors. If transceivers are located in-on-and-around the human body, radio propagation paths and their gains undergo large variations, especially when the polarization and orientation of antennas change with the body postures. Such variations are significant for microwaves because body dimensions are large compared to the wavelength. Thus, semi-analytical computational EM approaches are extremely useful to investigate the radio propagation around the human body and gain a deep insight into the underlying physics. On the contrary of the simplified theoretical model and analyses, numerical simulations can afford the simulation of very realistic and accurate scenarios based on the numerical phantoms presented in the previous section. In the following sections, we briefly outline wide-spread computational EM methods.

1) Ray Tracing: Scattering, reflection, and penetration are the three basic propagation phenomena to describe the interaction between the surrounding environment and the propagating waves. If the objects are larger than multiple signal wavelengths, ray tracing (RT) techniques can provide efficient and accurate results based on high-frequency asymptotic methods. Based on geometrical optics, the geometrical theory of diffraction (GTD) can calculate the reflected and refracted fields from and through surfaces [112]. Since it ignores the diffractions from curved surfaces and corners, GTD is inefficient in taking the multiple reflections into account, which can be mitigated by the uniform theory of diffraction (UTD) [113]. RT is highly popular, especially with the accurate and efficient calculation of key parameters, such as power delay profile (PDP), received signal strength, delay spread, and angle of arrival [92]. Therefore, RT techniques are also studied in body-centric communications [113]–[118].

2) Method of Moment: This method is developed to solve complex integrals by reducing them to a system of simpler linear equations using Harrington's weighted residuals techniques [119]. It is especially efficient for cases where volume is large compared to the surface such that solving Maxwell's equations over the entire volume of interest is not necessary. The Method of Moment (MoM) has a time complexity of $\mathcal{O}(N^2)$ and is not suitable for parallel computing methods [90], which limits its use to simple homogeneous geometries. Therefore, complexity poses considerable restrain on its application to IoB, where the received signal strength in/on the human body is required to be known. The MoM is mostly suitable for thin-wire structures and applicable in both time and frequency domains. Therefore, it is generally employed to study body propagation of loop wire antennas [120]–[124].

3) Finite Element Method: The finite element method (FEM) analyses EM structures by dividing them into a number of isoparametric elements in various shapes, e.g., rectangular and triangular. In this way, it is suitable for the propagation analysis of structures with curved boundaries. Since it is formulated by a set of linear equations, a major disadvantage of FEM is the time complexity of matrix solution. Denoting the number of rows and columns of stiffness matrix by the N and W, Farmaga *et al.* evaluated the complexity order of FEM as $\mathcal{O}(NW^2)$ [125], which turns out to be the highest among other numerical approaches. Since it is well-suited to MHz frequencies, it is mostly used for IoB applications operating at HBC frequencies [126]–[131] [see Section V-B2].

4) Finite-Difference Time-Domain: Since it was proposed by Yee in 1966 [132], finite-difference time-domain (FDTD) has become one of the best-known and widely-adopted numerical methods in computational EMs. Similar to FEM, it is capable of analyzing large, complex, and heterogeneous EM structures by dividing them into simpler elements. Unlike the high complexity of the previous methods, FDTD has a linear time complexity $\mathcal{O}(N)$ and suitable for parallel computing methods to handle large EM structures in finer resolutions [133]. However, this low complexity is at the expense of not being as flexible as the FEM method on curvy EM structures such as the human body [92]. The FDTD has found its place to model human head or entire body for SAR measurement purposes [134]–[138]. This method is also used in HBC application to measure the electric field around the human body [139]–[143]. It is shown in [141] and [142] that most of the electric field is concentrated around the tip and surface of the arm [see Section V-B2].

C. Summary and Insights

This section provided the fundamental insights into the EM properties (e.g., permittivity, conductivity, and permeability) and behaviors (e.g., absorption and penetration depth) of the human body. The tools and models presented help researchers gain a deeper understanding and perform accurate modeling of the propagation characteristics in-on-and-around the human body. Since dielectric properties are frequency dependent, overall propagation loss of in/on body links heavily depends on frequency, distance, and tissue properties along the propagation paths. Unlike the in-body links, the communication on and around the human body is jointly determined with EM interaction with the surrounding environment.

In order to validate the safety and characterize the channels, it is necessary to investigate EM interaction of IoB devices in a quantitative and precise manner. However, ethical constraints on conducting experiments on living subjects has led to the development of physical and numerical body phantoms that mimic the dielectric properties of the human body.

Accordingly, we surveyed physical (e.g., liquid, semi-liquid, semi-solid, and solid) and numerical (e.g., homogeneous and heterogeneous) phantoms in a comprehensive manner. Indeed, body phantoms are extensively used for SAR measurements and channel characterization especially for in/on body communication devices due to the technical challenges in locating transceivers inside the body [see Section IV]. The numerical body phantoms are particularly important for developing numerical propagation characterization methods, such as RT, MoM, FEM, and FDTD. FEM and FDTD have been mostly used to validate the analytical and empirical HBC channel models [see Section V].

IV. NB AND UWB CHANNEL MODELING

An accurate channel model is an initial and essential step for well-designed IoB communication and networking systems. However, modeling the communication channels within the proximity of the human body substantially differs from traditional communications. This is mainly because of the heterogeneous frequency-dependent dielectric nature of the human body that has relatively high permittivity and conductivity. Therefore, signal attenuation is mainly affected by the carrier frequency, the distance between transceivers as well as tissue dielectric properties along the propagation path, body curvatures, changing body postures, and so on.

For the sake of a better organization, we define three different IoB types based on their location on the human body.

- **I:** In-Body IoB nodes are either implanted or embedded devices located in deep tissues/organs or under the human skin, respectively;
- **O:** On-Body IoB nodes are located on or within 2-cm around the body surface;
- **E:** Off-Body IoB nodes are external devices located 2 cm to several meters away from the body surface;

which results in the following combination of link types: 1) **I/I:** In-Body to In-Body; 2) **I/O:** In-Body to On-Body; 3) **I/E:** In-Body to Off-Body; 4) **O/O:** On-Body to On-Body; and 5) **O/E:** On-Body to Off-Body. Depending on the IoB node location, the link budgets may be dominated by various channel characteristics. For example, in-body links (I/I and I/O) suffer from severe signal attenuation due to absorption and scattering effects of heterogeneous body tissues, whereas multipath fading and shadowing are more significant for on-body links (O/O and O/E) due to body postures, body movements, and reflecting surfaces in the surrounding environment. Of course, these links exhibit distinct behaviors at different node locations and frequency bands.

In the remainder of this section, we investigate NB and UWB channel modeling based on the first-order and the SOCs. While the first-order statistics account for mean and covariance of the signal attenuation, the second-order statistics are related to a variety of communication paradigms, such as delay spread, PDP, level-crossing rate (LCR), Doppler spread, auto-correlation and cross-correlation, and so on.

A. First-Order Channel Statistics

Based on the magnitude of variation in signal decay, the first-order channel statistic (FOCS) can be categorized into large-scale and small-scale signal attenuation. Hence, path loss and shadowing contribute to the large-scale FOCS, while multipath fading is the main reason for slight variations in the signal attenuation.

1) Large-Scale FOCS (Path Loss and Shadowing): The large-scale signal attenuation is mainly characterized by two phenomena: 1) absorption and 2) scattering. While the former is due to the lossy dielectric properties of body tissues, the latter is because of the heterogeneity of body tissues. On the other hand, shadowing is defined as random variations in signal decay and caused by creeping waves at low frequencies and diffractions existing in shadowed regions of the body surface.

Hence, large-scale fading is often presented as a combination of path loss and shadowing. Based on the empirical data obtained from channel measurements, the relation between path loss and channel distance is often represented by five different parametric models: the first and the most basic model assumes that path loss PL(d) [dB] linearly varies with distance d

$$\textbf{Model A: } \mathrm{PL}(d) = C + \alpha d + S \tag{1}$$

where d [m] is the distance between IoB nodes, C [dB] is a constant term that generally refers to the path loss at a reference distance, α is the slope parameter, and S [dB] is the log-normal shadowing component that follows a normal distribution with a standard deviation of σ_s, $S \sim \mathcal{N}(0, \sigma_s^2)$. In the second model, path loss varies with a power of the distance as follows:

$$\textbf{Model B: } \mathrm{PL}(d) = C + \alpha d^n + S \tag{2}$$

where n is the path loss exponent. The third model combines log-distance path loss model with log-normal shadowing for a given reference distance

$$\textbf{Model C: } \mathrm{PL}(d) = \mathrm{PL}(d_0) + 10n \log_{10}\left(\frac{d}{d_0}\right) + S \tag{3}$$

where PL(d_0) [dB] is the path loss at the reference distance d_0 [m]. Notice that (3) reduces to free-space radio propagation model for $n = 2$. The fourth model employs the following linear fitting model:

$$\textbf{Model D: } \mathrm{PL}(d) = \alpha \log_{10}(d) + \beta + S \tag{4}$$

where α and β are linear fitting coefficients. The last model follows an exponential decay that flattens out for large distance as a result of the contribution of multipath components from indoor environment:

$$\textbf{Model E: } \mathrm{PL}(d) = -10 \log_{10}(P_0 e^{-M_0 d} + P_1 e^{-M_1 d}) + S$$

where P_0 [dB] is the average loss close to the antenna; P_1 [dB] is the average attenuation of the transmitted signal that is reflected back by indoor environment; M_0 [dB/cm] is the average decay rate for the surface wave traveling around the perimeter of the body; and M_1 [dB/cm] is the average decay rate for reflected signals.

TABLE V
IN-BODY PARAMETRIC PATH LOSS MODELS

In-Body Parametric Path Loss Models					
Ref.	**Band**	**Frequency**	**Model**	**Link**	**Description**
[145]	MICS	402-405 MHz	Model C	I/I I/O	IEEE Std. 802.15.6
[149]	MICS WMTS ISM	402-405 MHz 863-870 MHz 2.4-2.5 GHz	Model C	I/I I/O	SIM: Finite integration technique EXP: Phantom Body
[150]	MICS ISM	402-405 MHz 2.4-2.5 GHz	Model D	I/O	EXP: Human/Phantom Body
[151]	ISM	2.4-2.5 GHz	Model A* Model C*	I/I I/O I/E	STAT: Liquid phantom
[152]	UWB	1-6 GHz	Model B	I/I	SIM: Finite integration technique
[153]	UWB	3.5-4.5 GHz	Model B	I/I	SIM: CST Studio software EXP: Pig tissues
[154]	UWB	3.4-4.8. GHz	Model C*	I/O	SIM: FDTD, EXP: Liquid Phantom
[155]	UWB	3.4-4.8. GHz	Model C	I/O	SIM: FDTD
[156]	UWB	2-6 GHz	Model C	I/I	SIM: Frequency dependent path loss based on FDTD simulations.

2) In-Body Link Budgets (I/I-I/O-I/E): The implanted IoB devices support a wide variety of medical applications, such as defibrillators, cardiac pacemakers, swallowable endoscopy capsules, glucose and bladder pressure monitors, smart pills for precise drug delivery to a target body location, and micro-robots used for the execution of biopsy and therapeutic procedures [144]. Due to ethical concerns and technical challenges, experimental in-body channel measurements are not possible on human subjects. Therefore, the implant channel characterization campaigns are carried out through measurements on experimental body phantoms or through simulations on numerical body phantoms, as explained in the previous section. There are two potential spectrum bands for in-body communication: 1) MICS and 2) lower UWB.

IEEE 802.15.6 standard allocated the MICS band for in-body links thanks to its favorable propagation behavior through human tissues and support for the use of small-size antennas. The Channel Modeling Subgroup of TG15.6 determined that Model C in (3) is a good fit for in-body channels. The mean value of in-body signal attenuation is caused by the lossy dielectric nature of human tissues whilst shadowing is because of the varying dielectric properties of different organs/tissues along the propagation path [19]. In order to obtain a statistical channel model, a 3-D immersive visualization and simulation platform is developed, and measurements are obtained for near-surface (cardiac pacemakers) and deep tissue (endoscopy capsule) devices [145]–[147].

Albeit having favorable in-body propagation characteristics, the limited bandwidth of MICS systems does not support high-speed communication. Hence, UWB systems have emerged as an attractive alternative with the following attributes [148]: as a result of the low maximum effective isotropic radiated power (EIRP) spectral density, the noise-like nature of UWB signals makes signal detection hard to unintended receivers. This inherent UWB feature increases the robustness of UWB systems against jamming, thereby mitigating the need for sophisticated encryption algorithms in low-cost transceivers [19]. Moreover, the simple structure impulse radio (IR) UWB transceivers facilitate miniature and low-power UWB systems. Table V lists different frequency bands and parametric path loss models used for I/I and I/O link configurations.

TABLE VI
ON-BODY PARAMETRIC PATH LOSS MODELS

On-Body Parametric Path Loss Models					
Ref.	**Band**	**Frequency**	**Model**	**Link**	**Description**
[158]	MICS WMTS ISM UWB	400-450 MHz 608-614 MHz 950-956 MHz 2.4-2.5 GHz 3.1-10.6 GHz	Model D	O/O	IEEE Std. 802.15.6 STAT: Body phantom meas. in hospital room and anechoic chamber.
[159]	ISM UWB	902-928 MHz 2.4-2.5 GHz 3.1-10.6 GHz	Model E Model C	O/O O/O	IEEE Std. 802.15.6 STAT: Body phantom meas.
[160]	ISM	2.4-2.5 GHz	Model C	O/O	STAT: Human body meas. SIM: FDTD
[161]	ISM	902-928 MHz 2.4-2.5 GHz	Model C Model E	O/O	STAT: Indoor human body meas.
[162]	UWB	3-6 GHz	Model C	O/O	STAT: Indoor human body meas.
[163]	UWB	3-6 GHz	Model C	O/O	STAT: Indoor human body meas.
[164]	UWB	4.2 GHz	Model C	O/O	STAT: Indoor human body meas.
[165]	UWB	3-10 GHz	Model C	O/O	STAT: Indoor human body meas.
[166]	UWB	2-8 GHz	Model C	O/O	STAT: Indoor human body meas.
[167]	UWB	3-6 GHz	Model C	O/O	STAT: Indoor human body meas.
[168]	UWB	3-10 GHz	Model C	O/O	STAT: Indoor human body meas.
[169]	UWB	3-6 GHz	Model C	O/O	STAT: Indoor human body meas.
[170]	UWB	3-9 GHz	Model D	O/O	STAT: Liquid phantom meas.
[171]	ISM	2.4-2.5 GHz	Model C	O/E	STAT: Indoor human body meas. with various body postures.
[172]	UWB	3-10 GHz	Model C	O/O	SIM: Distance and freq. depend.
[173]	ISM	2.4-2.5 GHz	Model C	O/E	STAT: Indoor human body meas. with various body postures.
[174]	UWB	2-10 GHz	Model C	O/E	STAT: Indoor human body meas. with various body postures.

3) On-Body Link Budgets (O/O-O/E): Unlike the regular outdoor and indoor RF channel characterization, propagation between two points on the human body has subtle distinctions. Although off-body communication (e.g., from an access point to a mobile handset) considers a sitting/standing person stationary, this is not a valid assumption for channel characterization between transceivers located on the human body. In addition to the environmental changes, the on-body link budgets also substantially differ from its off-body counterpart in being affected by the changes in body postures and gaits. For instance, the on-body link of a sitting person could be Line-of-Sight (LoS) or Nonline-of-Sight (NLoS) based on the body posture, which is generally considered the same in off-body channel characterization.

The parametric path loss models for the on-body links are tabulated in Table VI. Since technical and ethical restrictions of in-body communication do not apply for on-body communications, the majority of works consider statistical channel modeling. The experiments are often conducted in an indoor environment by measuring *S*-parameters using a fixed or hand-held vector network analyzer (VNA) if the human subject is stationary or mobile, respectively. The illustration of *S*-parameters measurement can be seen in Fig. 5. From all these statistical channel campaigns, one can infer that the following three critical factors have a significant impact on the measurements.

1) Although the parametric models capture the distance-dependent behavioral pattern, reported measurements highly depend on experimental setup and environment. Even measurement setups sharing the same parametric model within similar environments report a wide range of parameter values depending on the operational frequency and transceiver locations. For example, belt-to-chest, belt-to-head, belt-to-wrist links were, respectively, reported to have 38.9, 41, and 46.3 dB

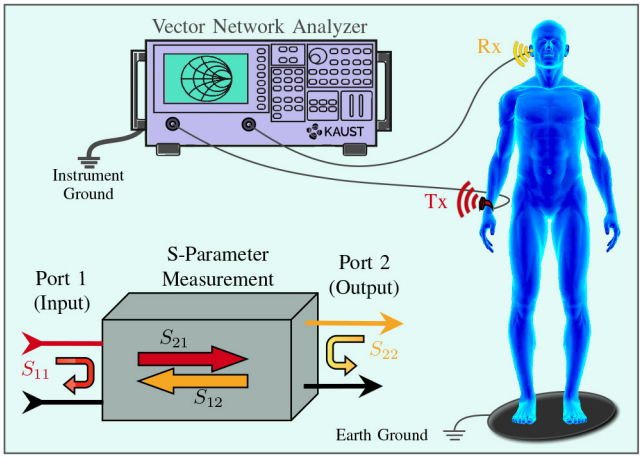

Fig. 5. Illustration of *S*-parameters measurements.

of average path-loss, which is proportional to the distance [14]. Notice that link fluctuations due to the changes in body postures and gaits become more significant during walking, running, and sports activities. For example, the peak-to-peak variation of the belt-to-chest link was recorded to be 8 and 21 dB during standing and moving scenarios, respectively. These variations were much higher for chest-to-head links, which were 44 and 56 dB in the stationary and mobile scenarios, respectively. It is even possible to observe around 4 dB variations due to involuntary body movements (e.g., breathing) [157]. Therefore, the generalization of these parametric models is not possible without a large parameter data set tailored to node locations and operational frequency.

2) Some of the works have recorded significant differences between measurements conducted within an anechoic chamber and daily-life indoor environments. This makes clear that multipath fading has an impact as noticeable as the large-scale fading. Therefore, anechoic chambers are necessary to strip the multipath fading component away and observe the large-scale fading alone.
3) Channel measurements are typically done by allowing transceivers to share the instrument ground of VNA [see Fig. 5]. This is hardly the case for wearable devices in practice and ignores the coupling effects. Although de-embedding antenna characteristics from propagation paths are generally neglected for on-body links, its momentous impacts on HBC channel characterization are thoroughly investigated [see Section V].

4) Small-Scale FOCS (Multipath Fading): As a result of body motions and posture changes, multiple paths are formed between the transmitter and receiver. Consequently, a received signal may end up as the superimposition of several delayed, attenuated, time-varying, and eventually distorted replicas of a transmitted signal [45]. The first-order small-scale statistical modeling studies mostly focus on on-body links as they are most vulnerable to multipath fading phenomena. Measured or simulated channel gain data is generally fitted to statistical distributions, which are commonly used to describe fading effects. These common small-scale fading distributions can be presented under the umbrella of generalized gamma distribution as follow:

$$f(x|a,b,c) = \frac{px^{ap-1}}{b^{ap}\Gamma(a)} \exp\left[-\left(\frac{x}{b}\right)^{p}\right] \tag{5}$$

where $\Gamma(\cdot)$ is the standard Gamma function, a and p are shape parameters, and b is the scale parameter. The generalized gamma distribution can reduce to the Rayleigh distribution ($p = 2$, $a = 1$), Nakagami-m distribution ($p = 2$), Weibull distribution ($a = 1$), and gamma distribution ($p = 1$), and log-normal distribution ($p \to 0$, $a = 2/(p^2 b^p)$). Based on more than 200 statistical fits, a comprehensive comparison of these distributions are provided in [20, and references therein]. Log-normal, Weibull, and gamma have been mostly studied and found often to be best fits. In particular, gamma/Weibull and log-normal/gamma distributions fit better to everyday and dynamic activities, respectively.

Although Nakagami-m, Rician, and Rayleigh distributions are commonly preferred to characterize small-scale fading in regular RF channels, they have been shown to provide poor fits for the on-body measurements [20]. This is again due to the aforementioned distinctions of communication on-and-around the human body. For NB channels, there is a general trend toward modeling small-scale fading by the Weibull and gamma distribution [175].

Since the channel gain is a product of numerous factors (e.g., diffraction, reflection, absorption, antenna gain, etc.), their contribution to the signal attenuation is additive in the log domain. Since the addition of multiple log-normally distributed paths still yields another log-normal distribution, log-normal distribution performs well to capture these multiplicative effects in additive dB scale. This is especially true for UWB channels with larger bandwidths. Therefore, in comparison to NB channels, the large-scale fading component is much higher for UWB channels due to higher frequencies [145]. This can also be observed for shadowing as shown in Tables V and VI.

In light of the above discussions, one can infer that small-scale fading statistics are also subject to node locations, dynamicity of the human body, carrier frequency, bandwidth, and surrounding environment. In order to decide on which statistical distribution is the best option for a specific scenario, potential distributions should be compared based on a "goodness-of-fit" criterion, which typically measures the discrepancy between observed values and the expected values under the target model. For instance, Akaike and Bayesian information criteria are two well-known tools that strike a balance between the fitness and simplicity of a model.

B. Second-Order Channel Statistics

FOCS concentrates on time-invariant components of the wireless channel and target mean/variance of the underlying distribution model. However, they are not sufficient to characterize the time-variant nature of channels. The propagation path on a walking/running human body randomly changes with time since the number of reflectors and their locations within the environment changes. This inevitably causes

random changes in delays, amplitudes, and multipath components. At this point, it is crucial to understand time-dependent variations of on-body links.

1) Delay Spread and Power Delay Profile: In multipath channels, the time delay spread is an important metric defined as the time between the first and the last received signal component of a transmitted signal. The delay spread is random especially for mobile terminals. For example, the propagation path of a left-wrist-to-right-hip link on a moving human subject randomly changes not only with the changing environment but also due to the swinging arms which expose and block LoS link. If the delay spread is smaller than the inverse of the bandwidth, then all multipath components (LoS and NLoS) are unresolvable, which is typically the case for NB signals. Fort *et al.* [161] investigated the root mean square (RMS) delay spread for 915 and 2.45 GHz with 15 and 45-cm antenna separations. They observe that the measured rms delay spreads are on the order of a few tens of ns in the worst case and it and follow a normal distribution.

For UWB signals, multipath components (LoS and NLoS) are generally resolvable since the delay spread is larger than the inverse of larger bandwidths. On the other hand, the PDP measures the intensity of a signal received through a multipath channel as a function of the time delay. In [163], the PDP of UWB channels is modeled as $p(\Delta\tau) = \alpha(\Delta\tau)^{\beta} + \gamma$ [dBm], where p is the signal power for each individual ray, $\Delta\tau$ is the excess delay with reference to the earliest arrival in ns, and (α, β, γ) are the fitting parameters. Fitting parameters based on measurements conducted along body-front and body-back are found to be $(-28.58, 0.431, -1.88)$ and $(-27.33, 0.492, 0.63)$, respectively. This can be interpreted as around 25 dBm signal strength loss over 1 ns delay duration. On the other hand, fitting parameters based on measurements conducted along front-torso and back-torso are found to be $(-5.13, 0, -24)$ and $(-7.79, 0, -22.43)$, respectively. That is, the PDP along the torso follows a linear behavior. The RMS and average PDP for in-body UWB links is studied in [152] where the RMS is shown to be less than 1 ns and the average PDP ranges from -5 to -30 dB.

Both delay spread and PDP determine the number of channel taps (i.e., significantly resolvable signal paths) and the presence of intersymbol interference (ISI). Unlike the NB channels, which are well approximated by a single tap [145], UWB channels are described by multiple taps as they are almost 50 times wider than NB channels specified by IEEE 802.15.6 [43]. Therefore, ISI has been mostly observed for UWB on-body channels [169], [176].

2) Level-Crossing Rate and Average Fade Duration: The LCR quantifies the rate at which the signal strength crosses a threshold, particularly at the mean path loss and usually in the positive-going direction. Thus, the LCR can be interpreted as a measure of the rapidity of the fading and often used to determine the Doppler spread as it is a function of the maximum Doppler shift. On the other hand, the average fade duration (AFD) is the average time the received signal is below a threshold and often used to measure the time during which packet losses occur on a link. Therefore, a longer AFD is not acceptable especially by URLLC applications. For a particular threshold value, the product of the AFD and the level crossing rate is a constant. Since they are closely related to speed and amount of body movement, they are both essential to characterize the channel dynamics [175].

In [164], the LCR and AFD were evaluated over the 3000 channel samples for threshold values ranging from -30 to 10 dB, which corresponds to 35 s of measurement. The LCR and AFD have been shown for links from center waist to: 1) head; 2) left-arm; 3) left-hand; and 4) chest. The measurements shows that LCR [Hz] has a bell shape whose peak value (around 8 Hz) is attained at -5 dB and -3 dB for links a–b and c–d, respectively. Interestingly, the skewness and kurtosis of LCR curves also changes significantly with link types, which emphasize the impact of node locations on the channel characteristics. On the other hand, the AFD of all links a-d is around 80 ms until -10 dB, which starts increasing exponentially and reach to 1 s at 8-dB approximately. Similar LCR and AFD measurements are also presented in [177] for various antenna types. On the other hand, the AFD of on-body links is also measured to be higher than 300 ms [178], which is above the 250-ms latency requirement of IEEE 802.15.6 [43].

3) Auto-Correlation: Autocorrelation of a time-variant channel determines the channel coherence time over which the channel impulse response is considered to be invariant. Thus, autocorrelation and AFD govern the duration of successful packet transmission both together. Therefore, they are key metrics to determine packet lengths, channel estimation pilot intervals, and frequency of updates to the power control [175]. While the coherence time of channel during daily activities have been reported to be up to 1 s, it reduces to 25–70 ms in case of significant and continuous body movement [175], [179]. The coherence time and coherence bandwidth are closely related and both determine the frequency-selective fading phenomenon. Hall *et al.* [14] roughly estimated the coherence bandwidth as 30 MHz based on 33 ns delay in a 5-m long room.

C. Antenna Effects

The antenna specifications at both transmitter and receiver side have a considerable impact on the overall channel gain. Unlike free space, the lossy dielectric nature of the human body alters the antenna features by shifting the resonant frequency, detuning impedance matching, modifying radiation pattern, and eventually reducing the overall efficiency [92]. Therefore, the measurements and statistical inferences provided by empirical studies must also consider the impact of antenna type and orientation on the measured attenuation levels.

For on-body links, there are two crucial requirements on antennas: 1) as a natural result of human body's influence on the antenna's reactive field and 2) the distance between antenna and body inherently determines the antenna matching attributes. Therefore, the first antenna requirement is being insensitive to the proximity of the human body. As discussed in Section III-A, the energy absorption and skin penetration depth reduces at high-frequency ranges, which yields distinct body-antenna interactions at NB and UWB channels. In the

NB case, the dominant and major drawback is strong mismatch caused by the resonance frequency shift, which destroys the overall antenna efficiency. A widely accepted approach to overcome this issue is employing adaptive impedance matching [180], [181]. On the contrary, the antenna proximity to the body slightly improves the impedance matching at UWB channels for two reasons: 1) the losses help the matching generally by lowering the S_{11} parameter and 2) the high permittivity tissues shifts the band down [183].

The second antenna requirement is having an optimal radiation pattern to minimize attenuation. In addition to antenna specifications, we previously explained that the channel quality is mainly determined by link geometry and antenna positions which determines the propagation mode (LoS, NLoS, creeping wave, etc.). In all these modes, the radiation pattern should be designed to minimize the propagation through-and-off body while maximizing the coupling between body-worn devices [14]. Such a design is nontrivial especially if one considers the large number of link geometry and body posture combinations.

Since the position or orientation of implant IoB cannot be controlled, omnidirectional in-body antennas are generally preferred to directional antennas to establish a reliable communication with a sensor array located on-or-off body [148]. For body-worn antennas, the radiation pattern must be omnidirectional in the horizontal plane and the polarization has to be vertical with respect to the human body [184]. For in-on-and-around the HBCs, a wide variety of antenna types are investigated, such as loop antennas, monopole/dipole antennas, and patch antennas [14], [154], [183], [184]. In addition to link loss-related issues, there are also other design parameters including endurance, miniaturization, low-profile, low-cost, light-weight, flexibility, comfortability, and ease of fabrication.

D. Summary and Insights

In this section, we begin with the FOCS which are mostly dealing with the mean and variance of the channel attenuation. The FOCS is further classified into two types: 1) large-scale and 2) small-scale fading. The mean and variance of the large-scale fading is mainly characterized by the path loss and shadowing, respectively. We presented five different parametric models which are commonly used to formulate composite path loss and shadowing effects. Accordingly, we tabulated in-body and on-body parametric path loss models in Tables V and VI, respectively. One can observe from Table V that most of the developed models are based on numerical phantoms and computational EM tools presented in Sections III-A and III-B, respectively. Although IEEE 802.15.6 determines the MICS band as the main channel for implant IoB nodes, there are also a considerable amount of works investigating UWB channels for in-body communications. On the other hand, on-body channels are mostly statistically characterized based on indoor measurements in general. A common observation across all works listed in Table VI is the discrepancies between reported values under various measurement setting. This is mainly because of the fact that on-body links can be in different propagation modes (LoS, NLoS, and creeping wave) which significantly varies with possibly large number of node locations and body postures combinations. Although reported works record conflicting parameter values, almost all of them share common parametric path loss models combined with log-normal shadowing. Unlike the in-body and HBC channels, the on-body NB and UWB links propagate in the air while being in interaction with the surrounding environment. Therefore, small-scale (multipath) fading is another important channel attributed that has been studied quite extensively. Log-normal, Weibull, and gamma distributions have been found to be the best fit, which contradicts with the regular RF channels (off-body) that are generally characterized by Rayleigh, Rician, and Nagakami-*m* fading.

Since the FOCS are not sufficient to capture the time-variant nature of human mobility, we also delve into the SOCS to shed light into the various communication phenomena, including delay spread, PDP, level crossing rate, AFD, channel coherence time and bandwidth, and auto-correlation. These are crucial statistics for cross-layer optimization of the IoB network architecture under dynamic channel conditions. Finally, we pointed out the impacts of antenna features on the channel attenuation measurements. Indeed, antenna radiation pattern and its proximity to the body has significant influence on shifting resonant frequency, detuning impedance matching, modifying radiation pattern, and finally reducing the overall efficiency. Therefore, it is necessary to quantify antenna gain along with other factors affected by the measurement set-up.

V. HBC Channel Modeling

In the previous section, we delved into the channel characteristics of in/on body wireless links where NB and UWB signals propagates in/around the human body. HBC is an alternative and promising wireless approach that uses human skin tissues as a communication channel, thus it is also referred to as body channel communication (BCC) or intrabody communication (IBC). HBC couples communication signals to the body through electro-static or magneto-static field via transmitter electrodes, which are captured by receiver electrodes on another part of the body. It is worth noting that such a communication is possible due to the bio-EM properties of the human body, which is covered in Section III-A.

The HBC channel is specifically confined to the frequency band between 100 and 100 MHz for two reasons [15]: 1) frequencies lover than 100 kHz is susceptible to all sort of EM interference and 2) at frequencies above 100 MHz, the human body acts as an antenna since the carrier wavelength reaches to the length of human body parts, where there is no longer HBC. This yields a carrierless communication scheme and decouples the transceiver size from the carrier wavelength. Operating on such low frequencies also have advantages in terms of modem complexity, power efficiency, physical layer security, safety, and so on.

In this section, we first provide an overview of three main coupling methods: 1) galvanic coupling (GC); 2) capacitive coupling (CC); and 3) magnetic coupling (MC). After that, we focus on channel characterization techniques which are based on analytical, numerical, circuit, and empirical models. Finally,

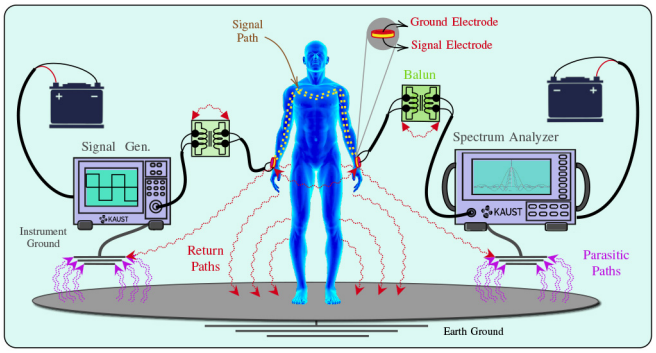

Fig. 6. Illustration of CC based HBC.

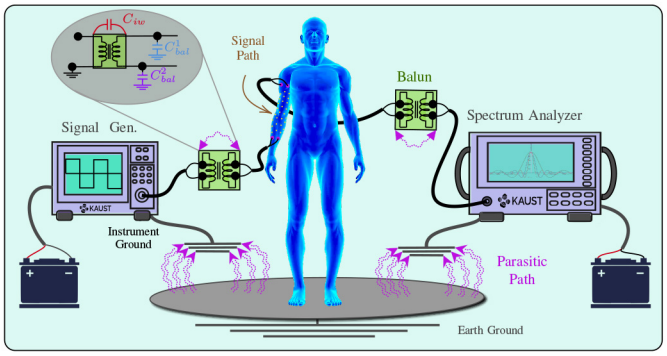

Fig. 7. Illustration of GC-based HBC.

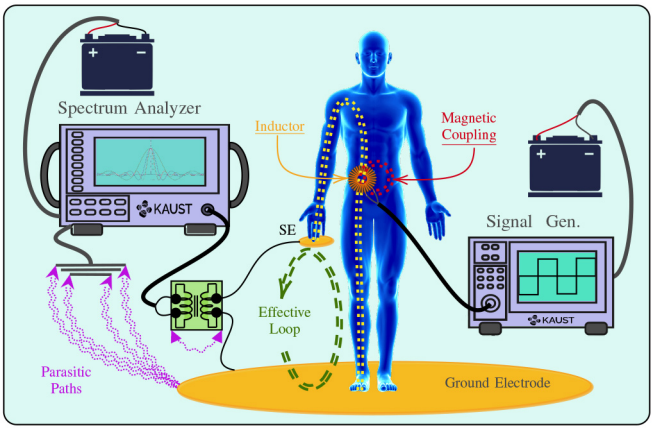

Fig. 8. Illustration of MC-based HBC.

we discuss how HBC channels are affected by human body movements and dynamics of the surrounding environment.

A. Overview of Coupling Methods

1) Capacitive Coupling: The CC, also known as near-field coupling or electro-static coupling, was first proposed for personal area networks by Zimmerman in 1995 [185]. The CC is illustrated in Fig. 6 where signal electrodes of both transmitter and receiver are attached to the skin whilst the ground electrodes are kept floating in air. The stimulated electric field on the signal electrode of the transmitter induces an electric flow on the signal path through the human body and a external return path through the surrounding environment (i.e., air). In other words, the conductivity of body not only generates the forward path but also creates a backward path by coupling electric field to the environment, the earth ground, and electrodes' ground plates [24]. For this very reason, the CC is more sensitive to environmental changes (e.g., appearance of nearby metallic objects and wires) and susceptible to interference caused by devices radiating electric fields.

2) Galvanic Coupling: The GC was first demonstrated where Handa *et al.* [186] coupled the modulated ECG signals to the human chest, that are received by a pair of electrodes on the wrist. The GC is illustrated in Fig. 7 where both signal and ground electrodes of transmitter and receiver are in contact with skin. On the contrary to CC, the GC is independent of environmental affects since the signal is mostly confined within the human body. GC is suitable for short distances ($\sim$ 15 - 40 cm) and low frequencies ($<$ 1 MHz), which restricts its suitability for QoS demanding applications [15]. Its stable and reliable channel conditions make the GC is a good option to periodically transmit physiological data especially using devices embedded underneath the skin [24].

3) Magnetic Coupling: Unlike CC and GC, MC exploits the EM resonance to generate a magneto quasi-static field throughout the body. As demonstrated in Fig. 8, the current induced by the signal flowing through the transmitter's coil (yellow dashed lines) generates a magnetic field (red dashed lines). When the foot and hand touch the ground and signal electrode at the same time, respectively, the conductive line and human body create a communication channel by forming an effective loop (green dashed lines) [187]. Notice that the communication channel disappears if foot or hand is detached from the electrodes. That is, the communication channel is connected and disconnected by closing and opening the effective loop, respectively. Similar to CC, MC can reach relatively long distances ($\sim$ 120 cm).

B. HBC Channel Models

An accurate channel model is essential for developing effective HBC systems. Nonetheless, this is a nontrivial task as HBC channels are affected by many factors, such as environment, distance between transceivers, electrode orientation and locations on the body, variable contact impedance of different electrode types and their specifications, and backward loss that dynamically changes with various body postures and movements.

1) Analytical Models: As discussed in Sections III-A and III-B, Maxwell's equations can explain the electric field within and around the body through a set of complex electric field equations. Therefore, analytical models have been developed to investigate the electric field based on EM theories [143], [188]–[190]. Bae *et al.* [189] considered three main electric field components of CC-HBC: 1) the quasi-static near field; 2) induction-field radiation; and 3) the surface wave field. The theoretical analysis is validated by measurements up to frequency of 100 MHz and channel distance of 1.3 m. A linear pathloss model [Model A in (1)] is also presented and compared with the FDTD-based linear model given in [143].

Teshome *et al.* [190] exploited multilayered ellipsoidal geometry to present a unified analytical GC-HBC channel model that can be used for any part of the body. The model is validated by FDTD simulations and phantom measurements. Similar to other works, pathloss has been shown to increase linearly with frequency and distance.

Wegmueller *et al.* [188] investigated GC-HBC by using FEM to understand the impacts of distance, tissue types, electrode positions, and joints on signal attenuation between 1 kHz and 1 MHz. The developed analytical models were compared with numerical simulations and *in-vivo* clinical trials. The results showed that a 5 cm increase in distance yields 6–9 dB more path loss while joints may put an additional 8 dB loss proportional to their size. Although receiver electrode size had a negligible effect, a larger transmitter size yielded a lower attenuation. The resistance of different tissues was also shown to have varying influence on the path loss.

2) Numerical Models: Among numerical tools presented Section III-B, there are two common methods used to simulate the signal propagation on HBC channels: 1) FEM [126]–[131] and 2) FDTD [139]–[143]. We refer interested readers to Section III-B for technical details of FEM and FDTD.

FEM: In [126], a circuit-coupled FEM method is used to explore CC-HBC. The FEM simulations on multilayer human forearm model is validated by clinical trials by using VNAs between 1–100 MHz. Results showed that increasing path loss by distance is mainly caused by the increasing length of the parasitic capacitor return path. The work in [126] is extended in [127] by dividing the surrounding environment into three regions: 1) near-field region; 2) transmission region; and 3) far-field region. A whole-body FEM simulations are conducted for GC-HBC in [128] where frequency-dependent signal attenuation has exhibits different slopes in low and high-frequency ranges. Moreover, the impact of distance on the frequency-dependent signal attenuation was also observed to become more significant as the frequency increases. A GC-HBC is also considered in [129] where the influence of frequency, channel length, and interelectrode distance have been analyzed. Specifically, authors have shown that attenuation increases as far as 20 dB for an increment of 5 cm and concluded that GC is limited to short distances. In [130], CC-HBC is investigated with different ground electrode heights, separation distances, and dimensions. During our initial investigations using FEM simulators, we observe that path loss exponentially decays with increasing frequency while its relation with distance is linear. We refer interested readers to [200] for a deeper insight into the FEM-based analysis and estimation of the GC-HBC channels.

Furthermore, the effects of different shapes and relative angles of the ground electrodes are investigated for the first time. The results have shown that a shape with more sides yields a smaller path loss. Interestingly, the authors conclude their simulation and experimental results with a path loss model which depends on air and ground coupling capacitances and electrode angles. Callejón [131] provided a computational GC-HBC analysis covering some issues that was not fully explained before, including the modeling of skin-electrode impedance, the differences associated with the use of constant voltage, current excitation modes, the influence of the subject's bioelectric properties on both distance and frequency-dependent attenuation.

TABLE VII
ANALYTICAL AND NUMERICAL HBC CHANNEL MODELS

		Ref.	Year	Coup.	Frequency	Pathloss	Validation Methods
Analytic		[188]	2009	GC	1 KHz-1MHz	Linear	SIM: Finite element Mesh EXP: In-vivo measure.
		[189]	2012	CC	1 KHz-100 MHz	Linear	EXP: Measure. up to 1.3 meters.
		[190]	2016	GC	<5 MHz	Linear	SIM: FDTD simulations EXP: Liquid Muscle Tissue Phantom
Numeric	FEM	[126]	2009	CC	1 MHz-100 MHz	-	EXP: In-vivo measure. (VNA)
		[127]	2011	CC	1 MHz-100 MHz	Linear*	EXP: In-vivo measure. (VNA)
		[128]	2012	GC	10 kHz–5 MHz	Linear*	EXP: In-vivo measure. (SG+OS)
		[129]	2014	GC	1 KHz-100 MHz	Linear	EXP: In-vivo measure. (SG+OS)
		[130]	2017	CC	1-40 MHz	Linear*	EXP: In-vivo measure. (VNA w. Balun)
	FDTD	[131]	2018	GC	<1 MHz	Linear*	EXP: In-vivo measure. (SG+OS w. Balun)
		[139]	2003	GC			
		[140]	2004	with	10 MHz	-	EXP: Tissue-equivalent solid phantom
		[141]	2006	single			
		[142]	2007	elect.			
		[143]	2009	pair	10-100 MHz	Linear	EXP: In-vivo measure. (SG+OS)

VNA: Vector Network Analyzer, SG: Signal generator, OS: Oscilloscope, *: Freq. dep. pathloss

FDTD: Fujii *et al.* [139], [140], [142] and Ito *et al.* [141] employed FDTD method for GC-HBC where a single pair of electrode is considered such that signal and ground electrodes act as transmitter and receiver, respectively. The simulation results are validated with measurements on tissue-equivalent solid phantom [143]. We refer interested readers to Table VII for a list of analytical and numerical HBC models.

3) Circuit Models: Previously discussed numerical models have two main drawbacks: 1) a long simulation time and 2) accuracy limited to low-frequency approximations of Maxwell's equations. Alternatively, circuit models offer shorter running times and accuracy for a wide range of frequencies. The circuit models are established on simple transfer functions that mathematically characterize the signal propagation along a transmission path on/in the human body [187], [191]–[199].

By using the frequency-dependent dielectric properties of different tissue types, a simple phantom can be modeled with resistance and capacitance, representing the dissipation loss, and charge holding ability of tissues, respectively. Since the human body parts are small compared to signal wavelengths under 100 MHz, the lumped-element model is capable of analyzing the signal behavior [198]. Accordingly, a variety of approaches have been developed, such as the use of a single RC model [187], longitudinal impedance model [194], 3-D circuit model [197], 5-tissue-layer circuit model [198], etc. Table VIII compare the circuit models based on frequency range, coupling method, equipment used for measurement, employed phantom/tissue model and types, propagation distance, and electrode specifications. The range of frequencies of interest and the coupling method are the main considerations to decide on the model that fits best the channel. To date, there is no standardized circuit model that characterizes the full human body over the entire HBC frequency range. This is mainly because of deteriorating accuracy level when generalization of a circuit model is not capable of accounting for various practical issues, which are discussed in the sequel.

The accuracy of the circuit models can be affected by several factors, such as conductive forward body path (CFP), capacitive backward path (CBP), propagation distance, dielectric properties of tissue layers, the signal radiation leaked to the air and absorbed by the body tissues, and electrode-skin

TABLE VIII
CIRCUIT MODELS

Circuit Models								
Ref.	**Circuit Model**		**CM**	**Equipment**	**P/T Model**	**CL [cm]**	**Electrode Specs.**	**P/T**
[187]	Single-lumped RC model	100 kHz–20 MHz	MC	SA, SG	A+CBP	-	10.5 × 7.5 cm 36.3 × 36.3 cm	S
[191]	RC type high-pass filter	100 kHz–150 MHz	CC	CCa, O, SA	A+T+CBP	10, 40, 120	d=1.5 cm	RH
[192]	Four-terminal circuit model	100 kHz–5 MHz	GC	O, SG	CFP+S+F+M+B+ BM +EEI+ESI	20, 30, 40	10 × 10 mm	A, L, H, T
[193]	Lossy transmission line without \emph{L}	*10–200 kHz 1–100 MHz	GC*, CC	BA, O, SA, SG	A+CBP	15–150	Copper electrodes with AgCl electrolyte	A
[194]	Longitudinal impedance model	200 kHz–10 MHz	GC	BA, VNA	S+F+M+CB	-	1 × 1 cm	S
[195]	Single-lumped RC blocks	1 MHz–100 MHz	CC	CCa, VNA	CFP+S+CBP	20, 30, 140	4-cm diameter circular	S
[196]	Mixed distributed-lumped element model	1 MHz–100 MHz	CC	LCR meter, VNA, CCa	T+ESI+EEI+TBI + CBP+CC+BA	15, 30, 140	Copper electrodes	A, C, T
[197]	3D circuit model	100 kHz–1 MHz	GC	O, SG	S+F+M+B+ C+ESI+S-F	0.2–1	10 × 10 × 1 mm, 0.5 × 0.5 cm	A
[198]	5-tissue-layer circuit model (serial and longitudinal admittances in parallel)	1 MHz–40 MHz	CC	BA, VNA	CFP+S+F+M+B+ BM+CBP+ESI	15, 30, 150	2 × 2 cm, 4 × 4 cm	A, L, T
[199]	A lumped bio-physical model	10 kHz–1 MHz	CC	O, SG	SG+E+S+P	20–25	Copper electrode	A, W
Legend	CM: Coupling Method, P: Phantom, T: Tissue, CL: Channel Length, d: diameter, A: Arm, RH: Right-Hand, L: Leg, H: Head, T: Torso, C: Chest, W: Wrist, S: Skin, F: Fat, M: Muscle, B: Bone, BM: Bone Marrow, C: Cell BA: Balun, CCa: Coaxial Cable, O: Oscilloscope. P:Probe, SA: Spectrum Analyzer, SG: Signal Generator, VNA: Vector Network Analyzer CC: Cap. Coupling, GC: Galv. Coupling, MC: Mag. Coupling, EEI: Electrode-Electrolyte Interface, ESI: Electrode-Skin Interface, TBI: Transceivers-Body Interference, CFP: Conductive Forward Path, CBP: Capacitive Backward Path							

contact/interface impedance. These effects are generally classified as intrinsic and extrinsic. The accuracy of a circuit models lies within the ability to account for intrinsic and extrinsic effects in the transfer functions. The intrinsic effects can be considered as static as they merely depend on channel distance and tissue properties along the propagation path rather than external/environmental conditions. On the contrary, the extrinsic effects are caused by the return and parasitic paths, as shown in Figs. 6 and 7. Furthermore, the interface between electrodes and skin is a significant part of the extrinsic channel as well as skin conditions, such as age and moisture level of the skin [198]. Based on the above discussion, one can tell that the intrinsic and extrinsic effects are more related to CFP and CBP, respectively. Indeed, one common observation on the presented models by references tabulated in Table VIII is that the accuracy decreases at higher frequency ranges, especially above 70 MHz.

4) Empirical Models: A common shortcoming of the previous channel models is that they cannot capture the impacts of environmental effects on the channel model. As a remedy, empirical models can provide a deeper insight into the channel behaviors under real circumstances. Figs. 6–8 depict different measurement setup by using various equipment, such as signal generator (SG), VNA, and spectrum analyzer (SA). However, recent studies have revealed that empirical studies reported significantly inconsistent channel gains due to different measurement configurations in terms of grounding, load resistance, the effect of cables and connections, and type of measurement devices [187], [191], [201]–[203], [211], [212]. We list the empirical studies in terms of these configurations in Table IX and discuss details in what follows.

a) Grounding effects: Using earth-grounded equipment leads to erroneous channel gain measurements since there is a cabled path between the measurement devices' internal grounds. In such a case, the true channel gain is overestimated as the measurement instruments' ground plane creates a larger path loss than the actual return path. In order to avoid such optimistic measurements, TX and RX ports have often been isolated from the common internal ground by using balanced-to-unbalanced (balun) components. In [199], the channel characteristic without baluns shows a flat band response with a loss of around 20 dB over the frequency range of 100–100 MHz. On the other hand, introducing baluns show a band-pass characteristic with a loss of ∼80 dB around 100 kHz and the minimum loss of ∼20 dB around 35 MHz. However, the use of baluns cause two types of parasitic paths [212].

1) As shown in Fig. 7, parasitic paths go through inter-winding capacitance ($C_{i\omega}$) that occur between balun terminals.
2) The differential signal influences the HBC channel by forming a return path through the surrounding environment. Thus, the asymmetrical capacitance between the ground and balun terminals should be the same in the whole frequency range. In this way, only parasitic paths from instrument's ground to the earth's ground will remain, as shown in Figs. 6 and 7.

Nonetheless, the use of baluns is not a complete solution to the grounding effects. In [201], it has been shown that the inclusion of any additional ground plane area overestimates the channel gain by up to 33.6 dB, whether it is isolated by via a balun or not. Therefore, recent studies considered battery-powered transceivers/instruments for a more accurate channel characterization [193], [196], [211].

b) Load resistance and instrument effects: Another critical concern on the experimental configuration is the input resistance of measurement instruments and transceivers. In the literature, measurement campaigns typically used 50 Ω and 1-MΩ load resistances [213]. Especially, in the case of GC-HBC, the impedance observed before and after the instruments is the same as that presented by the human body and electrode interface, which is independent of the frequency [129]. Therefore, 50 Ω may not be the best option for channel characterization. A comparison between 50 Ω and 1-MΩ load

TABLE IX
EMPIRICAL MODELS

Empirical Models															
Ref.	**VNA**		**SG**	**O**	**B**	**Cable Effects**	**Battery Powered**	**Ground Plane**	**# People**	**Env. Effects**	**Body Mov.**	**Electrode**	**CM**	**Frequency**	**Channel Length**
[191]	N	Y	-	Y	N	Y	Y	24–60 cm^2	1	Y	Y	d=1.5 cm	CC	100 kHz–150 MHz	10, 40, 120 cm
[201]	Y	Y	N	N	Y	Y	Y	4 × 4 × 3 m	1	–	N	30 × 30 mm^2	CC	20–150 MHz	20 cm
[202]	Y	N	N	N	Y/N	Y	Y/N	2.4 × 2.4 × 3 m	11	Y	Y	2 × 2 cm^2	GC	–	4, 16, 28, 36, 120 cm
[187]	N	Y	Y	N	N	-	N	36.5 × 36.5 cm	1	N	Y	7.5 × 10.5 cm^2	MC	⩽ 10 MHz	
[203]	N	N	Y	Y	N	Y	N	7×4 cm^2	94	–	N	2 × 2 cm^2	CC	⩽ 100 MHz	1.5 m
[204]	Y	N	N	N	Y	Y	–	–	4	Y	Y	3 × 3 cm^2 6 × 8 cm^2		300 kHz–15 MHz	30, 90, 150 cm
[195]	Y	N	-	-	Y	Y	N	–	1	–	N	2 × 2 cm^2	CC	1–100 MHz	5<d<150 cm
[205]	Y	N	Y	-	N	N	N	–	1	–	N	2 × 5 cm^2 2 × 10 cm^2		1 MHz–2.5 GHz	0.7<d<180 cm
[206]	Y	N	Y	N	N	–	N	–	1	–	Y	d=1 cm, 3cm	CC	200–600 MHz	20<d<155 cm
[207]	Y	N	N	N	Y	N	N	–	1	N	N	2 × 2 cm^2		10–100 MHz	15 cm
[208]	Y	N	N	Y	Y	Y	N	–	1	N	N	4 × 5 cm^2 4 × 10 cm^2	CC	1–100 MHz	20 cm
[209]	N	N	N	N	N	Y	Y	–	1	Y	Y	4 × 4 cm^2		100 kHz–60 MHz	11 cm
[188]	N	N	N	N	N	N	Y	–	2	N	N	28 × 20 cm^2 30 × 22 mm^2	GC	10 kHz–1 MHz	5 and 7 cm
[210]	N	Y	Y	N	N	N	Y	–	1	Y	Y	4 × 4 cm^2	CC	–	–
Legend:	VNA: Vector Network Analyzer, SA: Spectrum Analyzer, SG: Signal Generator, O: Oscilloscope, B: Balun Y:Yes, N:No, CM: Coupling Method, CC: Cap. Coupling, GC: Galv. Coupling, MG: Magnetive Coupling														

resistances shows that 1 MΩ yield a 25 dB more channel gain at 10 kHz, which reduces to 15 dB at 1 MHz [211]. It is also worth noting that VNAs, SGs, SAs, and oscilloscopes have different characteristics and thus different impacts on the measurements. In light of the above discussions, achieving optimum coupling is possible only if any impedance mismatch is avoided by taking the aforementioned issues into account.

c) Cable effects: The electrical cables are usually prone to attenuation and radiation at higher frequencies, which limits the range of study of the HBC channels. Therefore, their effect should be minimized as much as possible by using correct matching and minimal length. In the literature, several studies explored the cable effects [191], [195], [201]–[204], [207], [208], [211]. Various cable types are compared over 10 kHz to 100-MHz frequency range in [211], where the performance of computational and experimental results match well up to 1 MHz, then a difference about 10 dB observed starting from 4 MHz.

Excluding [203], the measurement campaigns carried out in references listed in Table IX with a limited number of participants, even some of them consider only a single-human subject. Since this inherently yields statistically insignificant results [202], [204]. To the best of the authors' knowledge, a holistic cross sectional and longitudinal study is yet to be performed to reach statistically meaningful inferences on the channel characteristics.

C. Variable Electrode-Skin Impedance

The electrode-skin (contact) impedance (ESI) between the human body and the signal electrode has a considerable impact on the overall path loss. The contact impedance is determined by the electrode-electrolyte interface (EEI) and the skin-surface impedance (SSI) track. While the EEI is characterized by electrode types (wet or dry) and specifications (size, shape, and metal), the SSI varies with operating frequency, skin conditions, and body motions. Therefore, the channel gains change with the contact impedance variations, which characterize the shadowing effects on HBC channels. In this section, we first introduce the circuit representation of ESI components and then discuss the impacts of electrode types (wet or dry) and specifications (size, shape, and metal) on the contact impedance.

1) Impacts of Electrode Types and Specifications: Similar to the role of antennas in the NB/UWB systems, electrodes have a major impact on the overall channel path loss as they are the main components that interface the human body and transceiver. Electrodes generally do not deliver the same performance as they come in a variety of designs, structures, materials, etc. In what follows, we first present electrode types and then discuss various specifications and their effects on the contact impedance.

a) Electrode types: Electrodes are broadly classified as wet and dry electrodes based on whether some chemical gels are used to increase the conductivity. The wet electrodes are further sorted into two types: 1) electrolyte and 2) pregelled electrodes. The latter offers a good fit and high conductivity and has a wide-spread use thanks to their disposable and low-cost nature [214]. However, the gel conductivity would degrade over prolonged use and/or through sweat/grease accumulation. This inherently deteriorates the overall transducer performance and limits the wet electrodes to single and short-term clinical use [215].

On the other hand, dry electrodes have a large contact impedance as it is a metal directly attached to the skin surface. The lack of a conductive gel causes two main problems: First, the air generally traps between the electrode and skin, which creates an extra dielectric layer and increases the overall impedance considerably. Second, the electrode may not attach well to a dry skin surface, which yields motion artifacts and high-contact impedance, as mentioned in the previous section. To overcome these drawbacks, dry electrodes are recently designed by using soft substrates, such as textile electrodes [216], tattoo electrodes [217], and skin-like electrodes [218] are popular examples of soft-electrodes. Since IoB nodes are generally used for long-term applications, dry electrodes are more suitable in terms of a longer

lifetime and reduced discomfort, which are vital attributes for commercialization efforts.

b) Electrode specifications: Material, size, and geometry of the electrodes are essential for the contact impedance's selectivity and sensitivity. In order to avoid irritation/discomfort to user skin and eliminate the performance deterioration over long-term use, electrode material should be biocompatibility and strike an excellent electrochemical balance at the ESI. Silver/silver chloride (Ag/AgCl) electrodes are widely accepted since they have stable chemical properties, low compensation voltage, low intrinsic noise, and low ESI [219]. Since Ag/AgCl electrodes have a simple and mature fabrication process, they also have a low cost [215]. In addition to the above Ag/AgCl electrode advantages, gold electrodes offer a better biocompatibility conductivity at a higher cost. Furthermore, metallic and carbon-based nanomaterials are also used in electrodes thanks to their advantages of having a large surface, higher conductivity, and better connectivity. For example, AgNW-based metal nanoparticle and nanowire electrodes are shown to deliver similar/superior performance with/than Ag/AgCl electrodes in resting/moving states [220].

The electrode size and geometry determine effective contact area, sensitivity, depth, and intensity of the applied electric field, and signal-to-noise ratio [221]. Electrodes typically come in rectangular, circular, spiral, ring, and interdigital shapes. While circular and rectangular electrodes are commonly macro-block electrodes, others are often microelectrodes. Along with the electrode size, interelectrode spacing also has a considerable impact on the penetration depth and electric field distribution [222].

2) Impedance Matching: Throughout the previous sections, our discussion concludes that modeling ESI is not trivial since it is affected by many factors, which inherently yields design uncertainty and degrades the connection reliability. The variable contact impedance also requires an extra margin at both the transmitter and receiver side, which results in an additional power budget. These necessitate impedance compensation techniques to maximize the power transfer at the electrode-to-skin interface [223], which can be done via matching networks [224]. At the cost of extra power margin, a commonly adopted way is increasing and decreasing the input and output impedance of the receiver and transceiver, respectively, [225]. A power-efficient alternative is adaptive and automatic receiver mode selection based on an impedance sensing circuit [226]. Tsou *et al.* [227] developed low and high modes to mitigate the variable contact impedance. The noncontact cases have been considered in [228] and [229], where an inductor is employed to compensate for the electrode-skin interface capacitance in a dynamic fashion.

D. Summary and Insights

Unlike the NB/UWB channels' coexistence and interference problems, the HBC is an alternative solution with the virtues of ultra low power operation, sufficient throughput for most of the IoB applications, and enhanced physical layer security due to the low signal leakage. In this section, we first outline three main coupling methods: 1) capacitive; 2) galvanic; and 3) magnetic. In the realm of HBC, CC-HBC, and GC-HBC are mostly preferred due to their practical use. While GC-HBC confines both forward and the backward path to the human body, the CC-HBC completes the backward path through the environment, the earth's ground, and electrodes' ground plates. For this reason, the CC-HBC is more sensitive to the environmental changes than the GC-HBC.

The HBC channels are characterized by analytical, numerical, circuit, and empirical models. Analytical models are important to gain a deep insight into the propagation mechanism by using a set of complex Maxwell's equations. For the sake of analytical tractability, analytical models are limited to simple cases. Therefore, analytical models found the basis of numerical methods, which run-heavy computational tools on numerical body phantoms presented in Section III-A. The FEM is the most common numerical technique to characterize the HBC channels. Numerical methods have a long simulation time and limited accuracy at low frequencies. Thus, circuit models are also developed based on an electric circuit representation of the human body's dielectric properties. A common shortcoming of these approaches is that they cannot capture the impacts of environmental effects on the channel model. As a remedy, empirical models can provide more realistic channel measurements. Nonetheless, the campaign measurements must be set very carefully as many factors affect the channel gain's true estimate, including grounding strategy, load resistance, instrumentation device specifications, and cable effects. Finally, the variable contact impedance yields design uncertainty and degrades the connection reliability. In order to avoid its negative impact on the overall HBC system performance, the contact impedance elements (e.g., ESI and SSI) should be accurately modeled and dynamically matched for the sake of improved performance.

VI. Conclusion and Future Research Directions

As an imminent extension to the IoT domain, IoB can open up significant opportunities, however, it is subject to technical challenges, security concerns, and risks. In this survey, we presented the IoB concept, specified requirements, and introduced related communications and networking standards. Then, we narrowed our scope to the characterization of channel features in-on-and-around the human body. A systematic survey of channel modeling issues is presented for various link types on NB, UWB, and HBC channels. In what follows, we bring prospective research directions to the interested readers' attention.

A. Unified Channel Models

In Sections IV and V, it has been clearly shown that reported channel attenuation statistics significantly differs from one article to another. This is mainly due to the enormous diversity of IoB communications in terms of channel length, operating frequency, propagation modes, a myriad combination of node locations and resulting link configurations, surrounding environment, hardware specifications, simulation methods, phantom types, and measurement set up. There is a dire need to have a unified channel model database which provides key

channel attributes based on frequency, distance, node locations, propagation mode, and surrounding environment. In this way, researchers and engineers can develop a more accurate system design that takes into consideration the impact of the hardware specifications (antenna matching and radiation, contact impedance of electrode, grounding effects, etc.). Although NB and UWB channel modeling issues have been studied more thoroughly, HBC channel modeling is relatively less explored. This is also the case for channel models provided by IEEE 802.15.6 [145] where HBC channels are briefly mentioned without getting into the technical details. Considering the distinct advantages offered by the HBC and the fact that it is less investigated, we see a window of opportunity for impactful contribution in this area.

B. Channel Estimation Techniques

Channel state information (CSI) is one of the most critical components to have efficient communication systems consisting of equalizers, demodulators, and decoders. The CSI can be categorized as instant and statistical. While the former describes the short-term channel response to optimize the performance by adapting the transmission scheme, the latter provides a long-term description for path loss, shadowing, fading distribution, prorogation mode, etc. In practice, the statistical CSI is used along with the instant CSI to represent a communication channel. Although CSI acquisition is a challenging task for fast fading channels, this is generally not the case for IoB nodes due to the limited speed of the human mobility.

One way for channel estimation is estimating the parameters of the statistical CSI models, i.e., estimating the parameters of the combined path-loss and shadowing models or estimating the shape, scale, and skewness parameters of the underlying fading distribution [230]. Another popular approach is periodically sending and analyzing pilot or training sequences which are known by both transmitter and receiver [231]. The accuracy of pilot-aided estimation can be further improved by iterative channel estimation by using the soft information inferred from the data symbols [232]. While the parameter estimation approach is suitable to update parameters of the statistical CSI, the pilot-aided estimation is more suitable to capture time-variant SOCS metrics. Recently, deep learning has been recognized as a powerful tool to improve overall channel estimation performance in comparison with the above traditional methods [233], [234]. Since the IoB nodes are not expected to have a high computational power, online learning approaches should be supported by offline training methods. An alternative approach would be striking a good balance between model-based and data-driven learning-based channel characterization.

C. Channel Aware Cross-Layer Optimization

Cross-layer network optimization is a key enabler of running a wide variety of IoB applications on limited network resources, some of which are already in the extensive use of other devices. As outlined in Section I-B, IoB applications have diverse QoS demands in terms of reliability, latency, energy efficiency, and data rate. Therefore, cross-layer optimization is a daunting challenge because of the human-body driven challenges discussed above and uncontrollable interference caused by the technologies coexisting on the same bands. The first and foremost prerequisite for an optimal cross-layer design is acquisition of accurate and timely channel estimates based on which the transmission scheme can control power, manage interference, and adapt necessary coding/modulation techniques [235]. The CSI is also necessary to have an adaptive design for two critical higher layer functions: 1) MAC to allow various IoB nodes to operate on the same band and 2) transmission control protocol to avoid congestion, sustain connectivity, and provision a reliable communication between the IoB node pairs. Body mobility and postures have already been shown to have substantial impacts on the key SOCS metrics, such as delay spread, PDP, level crossing rate, and AFD. To this end, we believe it is necessary to adapt MAC layer (e.g., packet length, frame structure, power control, channel estimation intervals, etc.) to such changes.

D. Energy Self-Sustainability & Network Lifetime

IoB nodes are naturally designed as ultralow power and low-cost devices with a limited battery capacity due to their small-form factor. However, they are still required to have a long operational time since either they are not reachable to charge (e.g., embedded or implanted IoB devices) or for the sake of user satisfaction (e.g., body worn devices). Therefore, energy harvesting is a key technology to design energy self-sustaining IoB devices by scavenging renewable energy sources, such as thermoelectric energy from body heat and kinetic energy from body motions. It is worth noting that a proper design is necessary to strike a good balance between power consumption and system performance based on QoS demands of underlying IoB application. In order to maximize the overall network lifetime, harvested energy must be used economically by means of energy efficient cross-layer approaches [236], which still depends on accurate channel estimation. There are two main factors contributing to the power consumption in IoB nodes.

Communication and signal processing circuitry are the most power-hungry part of the IoB devices. In addition to designing power-efficient circuit designs, energy-aware transmission strategies are of utmost importance, such as opportunistic transmission scheduling and lazy packet scheduling. As signal sampling and processing operations run more frequently than the signal transmission in the background, compressed sensing can significantly save energy in many IoB applications. Another major factor contributing to power consumption is the MAC protocol, which scales up the power consumed by communication and signal processing modules. Therefore, a power-wise MAC protocol should consider energy-efficient measures such as sleeping strategy for nodes exchanging data intermittently. The MAC should also minimize the number of retransmissions due to the collisions caused by interference received from nearby coexisting nodes at the same band. Considering the fact that all these approaches counts on a

precise CSI acquisition, it is obvious that channel characterization is critical to realize energy-efficient transmission and medium access schemes for energy self-sufficient IoB networks.

E. Opportunities in Millimeter-Wave Band

Thanks to its abundant bandwidth availability (3–300 GHz), millimeter Wave (mmWave) band has been considered to overcome spectrum scarcity of 5-GB cellular networks, in both access and backhaul link levels. Even if exiting standards do not recognize mmWave as a component of PHY layer, it has been has recently received substantial attention to be used in BANs [90]. Despite of its high bandwidth, mmWave band suffers from high propagation loss, need for directivity, and susceptibility to blockage, which makes it more suitable for LoS communication. Therefore, it could be a good-fit for on-body and off-body links rather than the implant in-body communications [237]. Since mmWave is expected to be well integrated in future wireless networks, we believe mmWave band can open up ample opportunity for IoB applications. However, unlike the PHY techniques surveyed in this article, there is no sufficient works on characterizing the mmWave channels on and around the human body.

F. Privacy and Security

Medical IoB applications necessitates a high level of security, confidentiality, and privacy [198]. IoB devices operating on NB and UWB channels are particularly susceptible to adversary nodes' capabilities of altering original data. Since these bands are already over-crowded by other communication devices, highly radiative and generally omni-directional nature of the NB and UWB communications inadvertently permits an eavesdropper to intercept the sensitive information. Accordingly, the confidentiality and privacy of transmitted data must be carefully guarded against the eavesdropping and overheard. Unfortunately, fulfilling these goals is a nontrivial task given the limited energy, memory, and computational power of IoB nodes.

Thanks to its low radiation footprint, HBC is inherently a viable alternative with its inherent physical layer security qualities. Since both forward and backward paths are confined within the body, the GC-HBC has a limited signal leakage compared to the CC-HBC technique. To further confine signals within the body, electro-quasistatic HBC (eQs-HBC) has recently proposed as a carrier-less (broadband) transmission [199]. Thereby, eQs-HBC creates a covert communication channel where it is extremely difficult for a nearby eavesdropper to intercept critical private data. The nominal work of Das *et al.* [239] revealed that eQs leakage is detectable up to < 0.15 m, whereas the human body alone leaks only up to $\sim$0.01 m. Compared to > 5 m detection range for on-body NB and UWB communication, this practically suggests that the adversary needs to be in direct physical contact with or almost touching the body to obtain any information.

REFERENCES

[1] L. Atzori, A. Iera, and G. Morabito, "The Internet of Things: A survey," *Comput. Netw.*, vol. 54, no. 15, pp. 2787–2805, 2010.

[2] I. F. Akyildiz and A. Kak, "The Internet of Space Things/CubeSats: A ubiquitous cyber-physical system for the connected world," *Comput. Netw.*, vol. 150, pp. 134–149, Feb. 2019.

[3] N. Saeed, M.-S. Alouini, and T. Y. Al-Naffouri, "Toward the Internet of Underground Things: A systematic survey," *IEEE Commun. Surveys Tuts.*, vol. 21, no. 4, pp. 3443–3466, 4th Quart., 2019.

[4] A. Celik, N. Saeed, B. Shihada, T. Y. Al-Naffouri, and M.-S. Alouini, "A software-defined opto-acoustic network architecture for Internet of Underwater Things," *IEEE Commun. Mag.*, vol. 58, no. 4, pp. 88–94, Apr. 2020.

[5] S. Jeschke, C. Brecher, T. Meisen, D. Özdemir, and T. Eschert, "Industrial Internet of Things and cyber manufacturing systems," in *Industrial Internet of Things: Cybermanufacturing Systems*, S. Jeschke, C. Brecher, H. Song, and D. B. Rawat, Eds. Cham, Switzerland: Springer Int., 2017, pp. 3–19, doi: 10.1007/978-3-319-42559-7_1

[6] A. Ometov, S. Bezzateev, J. Kannisto, J. Harju, S. Andreev, and Y. Koucheryavy, "Facilitating the delegation of use for private devices in the era of the Internet of Wearable Things," *IEEE Internet Things J.*, vol. 4, no. 4, pp. 843–854, Aug. 2017.

[7] P. Fraga-Lamas, T. M. Fernández-Caramés, M. Suárez-Albela, L. Castedo, and M. González-López, "A review on Internet of Things for defense and public safety," *Sensors*, vol. 16, no. 10, p. 1644, 2016.

[8] C. A. da Costa, C. F. Pasluosta, B. M. Eskofier, D. B. da Silva, and R. da Rosa Righi, "Internet of Health Things: Toward intelligent vital signs monitoring in hospital wards," *Artif. Intell. Med.*, vol. 89, pp. 61–69, Jul. 2018.

[9] B. Latré, B. Braem, I. Moerman, C. Blondia, and P. Demeester, "A survey on wireless body area networks," *Wireless Netw.*, vol. 17, no. 1, pp. 1–18, 2011.

[10] M. Maiti and U. Ghosh, "Next generation Internet of Things in FinTech ecosystem," *IEEE Internet Things J.*, early access, Mar. 3, 2021, doi: 10.1109/JIOT.2021.3063494.

[11] A. Milenković, C. Otto, and E. Jovanov, "Wireless sensor networks for personal health monitoring: Issues and an implementation," *Comput. Commun.*, vol. 29, nos. 13–14, pp. 2521–2533, 2006.

[12] L. Lorenzoni, A. Marino, D. Morgan, and C. James, "Health spending projections to 2030," OECD, Paris, France, Working Paper 110, 2019. [Online]. Available: https://doi.org/https://doi.org/10.1787/5667f23d-en

[13] "Novel Coronavirus 2019 Situation," orld Health Org., Geneva, Switzerland, Rep. 209, Jul. 2020.

[14] P. S. Hall *et al.*, "Antennas and propagation for on-body communication systems," *IEEE Antennas Propag. Mag.*, vol. 49, no. 3, pp. 41–58, Jun. 2007.

[15] H. Baldus, S. Corroy, A. Fazzi, K. Klabunde, and T. Schenk, "Human-centric connectivity enabled by body-coupled communications," *IEEE Commun. Mag.*, vol. 47, no. 6, pp. 172–178, Jun. 2009.

[16] H. Cao, V. Leung, C. Chow, and H. Chan, "Enabling technologies for wireless body area networks: A survey and outlook," *IEEE Commun. Mag.*, vol. 47, no. 12, pp. 84–93, Dec. 2009.

[17] M. Chen, S. Gonzalez, A. Vasilakos, H. Cao, and V. C. M. Leung, "Body area networks: A survey," *Mobile Netw. Appl.*, vol. 16, no. 2, pp. 171–193, 2011.

[18] S. Ullah *et al.*, "A comprehensive survey of wireless body area networks," *J. Med. Syst.*, vol. 36, no. 3, pp. 1065–1094, 2012.

[19] R. Chavez-Santiago *et al.*, "Propagation models for IEEE 802.15.6 standardization of implant communication in body area networks," *IEEE Commun. Mag.*, vol. 51, no. 8, pp. 80–87, Aug. 2013.

[20] D. B. Smith, D. Miniutti, T. A. Lamahewa, and L. W. Hanlen, "Propagation models for body-area networks: A survey and new outlook," *IEEE Antennas Propag. Mag.*, vol. 55, no. 5, pp. 97–117, Oct. 2013.

[21] M. Seyedi, B. Kibret, D. T. H. Lai, and M. Faulkner, "A survey on intrabody communications for body area network applications," *IEEE Trans. Biomed. Eng.*, vol. 60, no. 8, pp. 2067–2079, Aug. 2013.

[22] S. Movassaghi, M. Abolhasan, J. Lipman, D. B. Smith, and A. Jamalipour, "Wireless body area networks: A survey," *IEEE Commun. Surveys Tuts.*, vol. 16, no. 3, pp. 1658–1686, 3rd Quart., 2014.

[23] R. Cavallari, F. Martelli, R. Rosini, C. Buratti, and R. Verdone, "A survey on wireless body area networks: Technologies and design challenges," *IEEE Commun. Surveys Tuts.*, vol. 16, no. 3, pp. 1635–1657, 3rd Quart., 2014.

[24] J.-F. Zhao, X. M. Chen, B. D. Liang, and Q. Chen, "A review on human body communication: Signal propagation model, communication performance, and experimental issues," *Wireless Commun. Mobile Comput.*, vol. 2017, Oct. 2017, Art. no. 5842310. [Online]. Available: https://www.hindawi.com/journals/wcmc/2017/5842310/

[25] W. J. Tomlinson, S. Banou, C. Yu, M. Stojanovic, and K. R. Chowdhury, "Comprehensive survey of galvanic coupling and alternative intra-body communication technologies," *IEEE Commun. Surveys Tuts.*, vol. 21, no. 2, pp. 1145–1164, 2nd Quart., 2018.

[26] *Wireless LAN Medium Access Control (MAC) and Physical Layer (PHY) Specifications*, IEEE Standard 802.11-2016, pp. 1–3534, Dec. 2016.

[27] *Wireless LAN Medium Access Control (MAC) and Physical Layer (PHY) Specifications for Wireless Personal Area Networks (WPAN)*, IEEE Standard 802.15.1-2005, Jun. 2005.

[28] *IEEE Standard for Low-Rate Wireless Networks*, IEEE Standard 802.15.4-2015, pp. 1–709, Apr. 2016.

[29] *Specification of the Bluetooth System Version 5.1*, Bluetooth SIG, Kirkland, WA, USA, Jan. 2019.

[30] M. Hernandez and R. Kohno, "Coexistence of UWB-BANs with other wireless systems," in *Proc. Int. Symp. Intell. Signal Process. Commun. Syst.*, Jan. 2009, pp. 135–137.

[31] F. Martelli and R. Verdone, "Coexistence issues for wireless body area networks at 2.45 GHz," in *Proc. Eur. Wireless Conf.*, Apr. 2012, pp. 1–5.

[32] M. Hernandez and R. Miura, "Coexistence of IEEE std 802.15.6tm-2012 UWB-PHY with other UWB systems," in *Proc. IEEE Int. Conf. UWB*, Sep. 2012, pp. 46–50.

[33] ICNIRP Guideline, "Guidelines for limiting exposure to time-varying electric, magnetic, and electromagnetic fields (up to 300 ghz)," *Health Phys.*, vol. 74, no. 4, pp. 494–522, 1998.

[34] *Radio Frequency Safety*, Fed. Commissions Commun., Washington, DC, USA, 2019. [Online]. Available: https://www.fcc.gov/general/radio-frequency-safety-0

[35] *Potential Health Effects of Exposure to Electromagnetic Fields (EMF)*, Fed. Commissions Commun., Washington, DC, USA, 2015.

[36] V. S. Mallela, V. Ilankumaran, and N. S. Rao, "Trends in cardiac pacemaker batteries," *Indian Pacing Electrophysiol. J.*, vol. 4, no. 4, p. 201, 2004.

[37] A. M. Hussain and M. M. Hussain, "CMOS-technology-enabled flexible and stretchable electronics for Internet of Everything applications," *Adv. Mater.*, vol. 28, no. 22, pp. 4219–4249, 2016.

[38] M. Gao, L. Li, and Y. Song, "Inkjet printing wearable electronic devices," *J. Mater. Chem. C*, vol. 5, no. 12, pp. 2971–2993, 2017.

[39] C. C. Y. Poon, Y.-T. Zhang, and S.-D. Bao, "A novel biometrics method to secure wireless body area sensor networks for telemedicine and *m*-health," *IEEE Commun. Mag.*, vol. 44, no. 4, pp. 73–81, Apr. 2006.

[40] S. Cherukuri, K. K. Venkatasubramanian, and S. K. S. Gupta, "BIOSEC: A biometric based approach for securing communication in wireless networks of biosensors implanted in the human body," in *Proc. IEEE Int. Conf. Parallel Process. Workshops*, 2003, pp. 432–439.

[41] *ZigBee Specifications 05-3474-21*, ZigBee Alliance, Davis, CA, USA, Aug. 2015.

[42] *IPV6 Over Low Power WPAN (6LoWPAN)*, Internet Eng. Task Force, Fremont, CA, USA.

[43] *IEEE Standard for Wireless Body Area Networks*, IEEE Standard 802.15.6-2012, Feb. 2012.

[44] E. M. Staderini, "UWB radars in medicine," *IEEE Aerosp. Electron. Syst. Mag.*, vol. 17, no. 1, pp. 13–18, Jan. 2002.

[45] J. Wang and Q. Wang, *Body Area Communications: Channel Modeling, Communication Systems, and EMC*. New York, NY, USA: Wiley, 2012.

[46] H. Kanai, M. Haeno, and K. Sakamoto, "Electrical measurement of fluid distribution in legs and arms," *Medical Progress Through Technology: Medical engineering in Japan Research and Development*, K. Atsumi, F. Kajiya, T. Tsuji, and K. Tsujioka, Eds. Dordrecht, The Netherlands: Springer, 1987, pp. 159–170, doi: 10.1007/978-94-009-3361-3_14.

[47] C. Li *et al.*, *Principles and Applications of RF/Microwave in Healthcare and Biosensing*. Amsterdam, The Netherlands: Academic, 2016.

[48] H. P. Schwan, "Electrical properties of tissue and cell suspensions," in *Advances in Biological and Medical Physics*, vol. 5. London, U.K.: Elsevier, 1957, pp. 147–209.

[49] S. Gabriel, R. W. Lau, and C. Gabriel, "The dielectric properties of biological tissues: II. Measurements in the frequency range 10 hz to 20 GHz," *Phys. Med. Biol.*, vol. 41, no. 11, pp. 2251–2269, Nov. 1996.

[50] J. Wang, O. Fujiwara, and S. Watanabe, "Approximation of aging effect on dielectric tissue properties for sar assessment of mobile telephones," *IEEE Trans. Electromagn. Compat.*, vol. 48, no. 2, pp. 408–413, May 2006.

[51] B. Mohammed, A. Abbosh, B. Henin, and P. Sharpe, "Head phantom for testing microwave systems for head imaging," in *Proc. Cairo Int. Biomed. Eng. Conf. (CIBEC)*, 2012, pp. 27–39.

[52] Z. N. Chen, G. C. Liu, and T. S. P. See, "Transmission of RF signals between MICs loop antennas in free space and implanted in the human head," *IEEE Trans. Antennas Propag.*, vol. 57, no. 6, pp. 1850–1854, Jun. 2009.

[53] K. S. Moon, H. D. Choi, A. K. Lee, K. Y. Cho, H. G. Yoon, and K. S. Suh, "Dielectric properties of epoxy-dielectrics-carbon black composite for phantom materials at radio frequencies," *J. Appl. Polymer Sci.*, vol. 77, no. 6, pp. 1294–1302, 2000.

[54] S. Mochizuki *et al.*, "Effects of ear shape and head size on simulated head exposure to a cellular phone," *IEEE Trans. Electromagn. Compat.*, vol. 49, no. 3, pp. 512–518, Aug. 2007.

[55] V. Hombach, K. Meier, M. Burkhardt, E. Kuhn, and N. Kuster, "The dependence of EM energy absorption upon human head modeling at 900 MHz," *IEEE Trans. Microw. Theory Techn.*, vol. 44, no. 10, pp. 1865–1873, Oct. 1996.

[56] K. Ogawa and T. Matsuyoshi, "An analysis of the performance of a handset diversity antenna influenced by head, hand, and shoulder effects at 900 Mhz. I. Effective gain characteristics," *IEEE Trans. Veh. Technol.*, vol. 50, no. 3, pp. 830–844, May 2001.

[57] F. Zhang, X. Liu, S. A. Hackworth, R. J. Sclabassi, and M. Sun, "*In vitro* and *in vivo* studies on wireless powering of medical sensors and implantable devices," in *Proc. IEEE/NIH Life Sci. Syst. Appl. Workshop*, 2009, pp. 84–87.

[58] S.-I. Watanabe, H. Taki, T. Nojima, and O. Fujiwara, "Characteristics of the sar distributions in a head exposed to electromagnetic fields radiated by a hand-held portable radio," *IEEE Trans. Microw. Theory Techn.*, vol. 44, no. 10, pp. 1874–1883, Oct. 1996.

[59] T. Kobayashi, T. Nojima, K. Yamada, and S. Uebayashi, "Dry phantom composed of ceramics and its application to sar estimation," *IEEE Trans. Microw. Theory Techn.*, vol. 41, no. 1, pp. 136–140, Jan. 1993.

[60] H. Tamura, Y. Ishikawa, T. Kobayashi, and T. Nojima, "A dry phantom material composed of ceramic and graphite powder," *IEEE Trans. Electromagn. Compat.*, vol. 39, no. 2, pp. 132–137, May 1997.

[61] V. Monebhurrun, "Conservativeness of the SAM phantom for the SAR evaluation in the child's head," *IEEE Trans. Magn.*, vol. 46, no. 8, pp. 3477–3480, Aug. 2010.

[62] O. A. Saraereh, M. Jayawardene, P. McEvoy, and J. C. Vardaxoglou, "Simulation and experimental SAR and efficiency study for a dual-band PIFA handset antenna (GSM 900 / DCS 1800) at varied distances from a phantom head," in *Proc. IEE Antenna Meas. SAR (AMS)*, 2004, pp. 5–8, doi: 10.1049/ic:20040066.

[63] C. K. Looi and Z. N. Chen, "Design of a human 'head' equivalent phantom for ISM 2.4-Ghz applications," *Microw. Opt. Technol. Lett.*, vol. 47, no. 2, pp. 163–166, Oct. 2005.

[64] C. K. Looi, T. S. P. See, and Z. N. Chen, "Study of human head effects on the planar inverted-F antenna," in *Proc. IEEE Int. Workshop Antenna Tech. Small Antennas Novel Metamater. (IWAT)*, 2005, pp. 223–226, doi: 10.1109/IWAT.2005.1461055.

[65] I. J. Youngs, A. S. Treen, G. Fixter, and S. Holden, "Design of solid broadband human tissue simulant materials," *IEE Proc. Sci. Meas. Technol.*, vol. 149, no. 6, pp. 323–328, Jan. 2002.

[66] K. Ito, Y. Okano, A. Hase, and I. Ida, "A tissue-equivalent solid phantom for estimation of interaction between human head and handset antenna," in *Proc. IEEE-APS Conf. Antennas Propag. Wireless Commun.*, 1998, pp. 89–92, doi: 10.1109/APWC.1998.730662.

[67] A. T. Mobashsher, A. M. Abbosh, and Y. Wang, "Microwave system to detect traumatic brain injuries using compact unidirectional antenna and wideband transceiver with verification on realistic head phantom," *IEEE Trans. Microw. Theory Techn.*, vol. 62, no. 9, pp. 1826–1836, Sep. 2014.

[68] A. T. Mobashsher and A. M. Abbosh, "Three-dimensional human head phantom with realistic electrical properties and anatomy," *IEEE Antennas Wireless Propag. Lett.*, vol. 13, pp. 1401–1404, 2014.

[69] B. J. Mohammed, A. M. Abbosh, S. Mustafa, and D. Ireland, "Microwave system for head imaging," *IEEE Trans. Instrum. Meas.*, vol. 63, no. 1, pp. 117–123, Jan. 2014.

[70] B. J. Mohammed and A. M. Abbosh, "Realistic head phantom to test microwave systems for brain imaging," *Microw. Opt. Technol. Lett.*, vol. 56, no. 4, pp. 979–982, 2014.

[71] S. Mustafa, B. Mohammed, and A. Abbosh, "Novel preprocessing techniques for accurate microwave imaging of human brain," *IEEE Antennas Wireless Propag. Lett.*, vol. 12, pp. 460–463, 2013.

[72] A. T. Mobashsher, B. J. Mohammed, S. Mustafa, and A. Abbosh, "Ultra wideband antenna for portable brain stroke diagnostic system," in *Proc. IEEE IMWS-BIO*, 2013, pp. 1–3.

[73] H. Schwerdt, J. Chae, and F. Miranda, "Wireless performance of a fully passive neurorecording microsystem embedded in dispersive human head phantom," in *Proc. IEEE Int. Symp. Antennas Propag.*, 2012, pp. 1–2.

[74] H. N. Schwerdt, F. A. Miranda, and J. Chae, "A fully passive wireless backscattering neurorecording microsystem embedded in dispersive human-head phantom medium," *IEEE Electron Device Lett.*, vol. 33, no. 6, pp. 908–910, Jun. 2012.

[75] R. Ishido, "A study in the solid phantom for 3–6 GHz and evaluation of SAR distribution based on the thermographic method," in *Proc. EMC*, 2004, pp. 80–83.

[76] G. A. Conway, W. G. Scanlon, C. Orlenius, and C. Walker, "*In situ* measurement of UHF wearable antenna radiation efficiency using a reverberation chamber," *IEEE Antennas Wireless Propag. Lett.*, vol. 7, pp. 271–274, 2008.

[77] G. Conway, W. Scanlon, and S. Cotton, "The performance of on-body wearable antennas in a repeatable multipath environment," in *Proc. IEEE Antennas Propag. Soc. Int. Symp.*, 2008, pp. 1–4.

[78] G. Gajda, M. A. Stuchly, and S. S. Stuchly, "Mapping of the near-field pattern in simulated biological tissues," *Electron. Lett.*, vol. 15, no. 4, pp. 120–121, Feb. 1979.

[79] A. Cheung and D. Koopman, "Experimental development of simulated biomaterials for dosimetry studies of hazardous microwave radiation (short papers)," *IEEE Trans. Microw. Theory Techn.*, vol. MTT-24, no. 10, pp. 669–673, Oct. 1976.

[80] T. Yamamoto *et al.*, "Development of electromagnetic phantom at low-frequency band," in *Proc. IEEE Int. Conf. Eng. Med. Biol. Soc.*, 2013, pp. 1887–1890.

[81] H. Kato and T. Ishida, "Development of an agar phantom adaptable for simulation of various tissues in the range 5–40 MHz. (hyperthermia treatment of cancer)," *Phys. Med. Biol.*, vol. 32, no. 2, pp. 221–226, Jan. 1987.

[82] G. Hartsgrove, A. Kraszewski, and A. Surowiec, "Simulated biological materials for electromagnetic radiation absorption studies," *Bioelectromagnetics*, vol. 8, no. 1, pp. 29–36, 1987.

[83] V. Vigneras and F. Bonnaudin, "Biological tissues equivalent liquids in the frequency range 900–3000 MHz," in *Proc. XXVIIIth URSI Gen. Assembly*, 2005, pp. 1–4.

[84] T. Takimoto, T. Onishi, K. Saito, M. Takahashi, S. Uebayashi, and K. Ito, "Characteristics of biological tissue equivalent phantoms applied to UWB communications," *Electron. Commun. Japan Commun.*, vol. 90, no. 5, pp. 48–55, 2007.

[85] Y. Yuan *et al.*, "A heterogeneous human tissue mimicking phantom for RF heating and MRI thermal monitoring verification," *Phys. Med. Biol.*, vol. 57, no. 7, pp. 2021–2037, 2012.

[86] C. Gabriel, "Tissue equivalent material for hand phantoms," *Phys. Med. Biol.*, vol. 52, no. 14, pp. 4205–4210, 2007.

[87] N. Chahat, M. Zhadobov, and R. Sauleau, "Broadband tissue-equivalent phantom for BAN applications at millimeter waves," *IEEE Trans. Microw. Theory Techn.*, vol. 60, no. 7, pp. 2259–2266, Jul. 2012.

[88] N. Chahat, C. Leduc, M. Zhadobov, and R. Sauleau, "Antennas and interaction with the body for body-centric wireless communications at millimeter-waves," in *Proc. IEEE Eur. Conf. Antennas Propag.*, 2013, pp. 772–775.

[89] L. Zhang, Z. Wang, and J. L. Volakis, "Textile antennas and sensors for body-worn applications," *IEEE Antennas Wireless Propag. Lett.*, vol. 11, pp. 1690–1693, 2012.

[90] A. Pellegrini *et al.*, "Antennas and propagation for body-centric wireless communications at millimeter-wave frequencies: A review [wireless corner]," *IEEE Antennas Propag. Mag.*, vol. 55, no. 4, pp. 262–287, Aug. 2013.

[91] T. Cuyckens, "Influence of the human body on the behaviour of monopole and patch antennas," Ph.D. dissertation, Dept. Elect. Eng., Ghent Univ., Ghent, Belgium, 2010.

[92] P. S. Hall and Y. Hao, *Antennas and Propagation for Body-Centric Wireless Communications*. London, U.K.: Artech House, 2012.

[93] A. E. Khorshid, I. N. Alquaydheb, A. M. Eltawil, and F. J. Kurdahi, "Physical multi-layer phantoms for intra-body communications," *IEEE Access*, vol. 6, pp. 42812–42821, 2018.

[94] A. E. Khorshid *et al.* "IBCFAP: Intra-body communications five-layers arm phantom model," *IEEE Access*, vol. 7, pp. 93701–93710, 2019.

[95] A. W. Guy, "Analyses of electromagnetic fields induced in biological tissues by thermographic studies on equivalent phantom models," *IEEE Trans. Microw. Theory Techn.*, vol. MTT-19, no. 2, pp. 205–214, Feb. 1971.

[96] C.-K. Chou, G.-W. Chen, A. W. Guy, and K. H. Luk, "Formulas for preparing phantom muscle tissue at various radiofrequencies," *J. Bioelectromagn. Soc.*, vol. 5, no. 4, pp. 435–441, 1984.

[97] N. Chahat, M. Zhadobov, S. Alekseev, and R. Sauleau, "Human skin-equivalent phantom for on-body antenna measurements in 60 GHz band," *Electron. Lett.*, vol. 48, no. 2, pp. 67–68, 2012.

[98] M. Mazzurana, L. Sandrini1, A. Vaccari, C. Malacarne, L. Cristoforetti, and R. Pontalti, "A semi-automatic method for developing an anthropomorphic numerical model of dielectric anatomy by MRI," *Phys. Med. Biol.*, vol. 48, no. 19, pp. 3157–3170, Sep. 2003.

[99] H. N. Kritikos and H. P. Schwan, "Hot spots generated in conducting spheres by electromagnetic waves and biological implications," *IEEE Trans. Biomed. Eng.*, vol. BME-19, no. 1, pp. 53–58, Jan. 1972.

[100] A. R. Shapiro, R. F. Lutomirski, and H. T. Yura, "Induced fields and heating within a cranial structure irradiated by an electromagnetic plane wave," *IEEE Trans. Microw. Theory Techn.*, vol. MTT-19, no. 2, pp. 187–196, Feb. 1971.

[101] W. T. Joines and R. J. Spiegel, "Resonance absorption of microwaves by the human skull," *IEEE Trans. Biomed. Eng.*, vol. BME-21, no. 1, pp. 46–48, Jan. 1974.

[102] C. M. Weil, "Absorption characteristics of multilayered sphere models exposed to UHF/microwave radiation," *IEEE Trans. Biomed. Eng.*, vol. BME-22, no. 6, pp. 468–476, Nov. 1975.

[103] H. Massoudi, C. H. Durney, P. W. Barber, and M. F. Iskander, "Electromagnetic absorption in multilayered cylindrical models of man," *IEEE Trans. Microw. Theory Techn.*, vol. MTT-27, no. 10, pp. 825–830, Oct. 1979.

[104] S. Nishizawa and O. Hashimoto, "Effectiveness analysis of lossy dielectric shields for a three-layered human model," *IEEE Trans. Microwave Theory Techn.*, vol. 47, no. 3, pp. 277–283, Mar. 1999.

[105] C. WG3, "Proposal for numerical canonical models in mobile communications," 1994.

[106] A. Christ *et al.*, "The virtual family—Development of surface-based anatomical models of two adults and two children for dosimetric simulations," *Phys. Med. Biol.*, vol. 55, no. 2, p. N23, 2009.

[107] M.-C. Gosselin *et al.*, "Development of a new generation of high-resolution anatomical models for medica L device evaluation: The virtual population 3.0," *Phys. Med. Biol.*, vol. 59, no. 18, pp. 5287–5303, Aug. 2014.

[108] N. Petoussi-Henss, M. Zanki, U. Fill, and D. Regulla, "The GSF family of voxel phantoms," *Phys. Med. Biol.*, vol. 47, no. 1, p. 89, 2001.

[109] C. Waldby, *The Visible Human Project: Informatic Bodies and Posthuman Medicine*. New York, NY, USA: Psychol., 2000.

[110] T. Nagaoka *et al.*, "Development of realistic high-resolution whole-body voxel models of japanese adult males and females of average height and weight, and application of models to radio-frequency electromagnetic-field dosimetry," *Phys. Med. Biol.*, vol. 49, no. 1, p. 1, 2003.

[111] T. Wu *et al.*, "Chinese adult anatomical models and the application in evaluation of rf exposures," *Phys. Med. Biol.*, vol. 56, no. 7, p. 2075, 2011.

[112] J. B. Keller, "Geometrical theory of diffraction," *J. Opt. Soc. America*, vol. 52, no. 2, pp. 116–130, 1962.

[113] M. Ghaddar, L. Talbi, T. A. Denidni, and A. Sebak, "A conducting cylinder for modeling human body presence in indoor propagation channel," *IEEE Trans. Antennas Propag.*, vol. 55, no. 11, pp. 3099–3103, Nov. 2007.

[114] M. Ghaddar, L. Talbi, T. Denidni, and A. Charbonneau, "Modeling human body effects for indoor radio channel using UTD," in *Proc. IEEE Can. Conf. Elect. Comput. Eng.*, vol. 3, 2004, pp. 1357–1360.

[115] D. S. Ahluwalia, "Uniform asymptotic theory of diffraction by the edge of a three-dimensional body," *SIAM J. Appl. Math.*, vol. 18, no. 2, pp. 287–301, 1970.

[116] Y. Zhao *et al.*, "UWB on-body radio channel modeling using ray theory and subband fdtd method," *IEEE Trans. Microw. Theory Techn.*, vol. 54, no. 4, pp. 1827–1835, Jun. 2006.

[117] S. Collonge, G. Zaharia, and G. E. Zein, "Influence of the human activity on wide-band characteristics of the 60 GHz indoor radio channel," *IEEE Trans. Wireless Commun.*, vol. 3, no. 6, pp. 2396–2406, Nov. 2004.

[118] G. Koutitas, "Multiple human effects in body area networks," *IEEE Antennas Wireless Propag. Lett.*, vol. 9, pp. 938–941, 2010.

[119] R. F. Harrington, *Field Computation by Moment Methods*. Hoboken, NJ, USA: Wiley, 1993.

[120] K. Ito, I. Ida, and M.-S. Wu, "Body effect on characteristics of small loop antenna in pager systems," in *Proc. IEEE Antennas Propag. Soc. Int. Symp.*, 1992, pp. 1081–1084.

[121] H.-R. Chuang and W.-T. Chen, "Computer simulation of the human-body effects on a circular-loop-wire antenna for radio-pager communications at 152, 280, and 400 MHz," *IEEE Trans. Veh. Technol.*, vol. 46, no. 3, pp. 544–559, Aug. 1997.

[122] D. Psychoudakis *et al.*, "Body-worn diversity antennas for squad area networks (SAN)," in *Proc. URSI Gen. Assembly*, 2008, pp. 1–4.

[123] W.-T. Chen and H.-R. Chuang, "Numerical computation of human interaction with arbitrarily oriented superquadric loop antennas in personal communications," *IEEE Trans. Antennas Propag.*, vol. 46, no. 6, pp. 821–828, Jun. 1998.

[124] W.-T. Chen and H.-R. Chuang, "Numerical computation of the em coupling between a circular loop antenna and a full-scale human-body model," *IEEE Trans. Microw. Theory Techn.*, vol. 46, no. 10, pp. 1516–1520, Oct. 1998.

[125] I. Farmaga *et al.*, "Evaluation of computational complexity of finite element analysis," in *Proc. Int. Conf. Exp. Design. Appl. CAD Syst. Microelectron.*, 2011, pp. 213–214.

[126] R. Xu, H. Zhu, and J. Yuan, "Circuit-coupled fem analysis of the electric-field type intra-body communication channel," in *Proc. IEEE Biomed. Circuits Syst. Conf.*, 2009, pp. 221–224.

[127] R. Xu, H. Zhu, and J. Yuan, "Electric-field intrabody communication channel modeling with finite-element method," *IEEE Trans. Biomed. Eng.*, vol. 58, no. 3, pp. 705–712, Mar. 2011.

[128] Y. Song *et al.*, "A finite-element simulation of galvanic coupling intra-body communication based on the whole human body," *Sensors*, vol. 12, no. 10, pp. 13567–13582, 2012.

[129] M. A. Callejón, J. Reina-Tosina, D. Naranjo-Hernández, and L. M. Roa, "Galvanic coupling transmission in intrabody communication: A finite element approach," *IEEE Trans. Biomed. Eng.*, vol. 61, no. 3, pp. 775–783, Mar. 2014.

[130] J. Mao, H. Yang, and B. Zhao, "An investigation on ground electrodes of capacitive coupling human body communication," *IEEE Trans. Biomed. Circuits Syst.*, vol. 11, no. 4, pp. 910–919, Aug. 2017.

[131] M. A. Callejon *et al.*, "A parametric computational analysis into galvanic coupling intrabody communication," *IEEE J. Biomed. Health Inform.*, vol. 22, no. 4, pp. 1087–1096, Jul. 2018.

[132] K. Yee, "Numerical solution of initial boundary value problems involving maxwell's equations in isotropic media," *IEEE Trans. Antennas Propag.*, vol. 14, no. 3, pp. 302–307, May 1966.

[133] A. Taflove and S. C. Hagness, *Computational Electrodynamics: The Finite-Difference Time-Domain Method*. London, U.K.: Artech House, 2005.

[134] J.-Y. Chen and O. P. Gandhi, "Currents induced in an anatomically based model of a human for exposure to vertically polarized electromagnetic pulses," *IEEE Trans. Microw. Theory Techn.*, vol. 39, no. 1, pp. 31–39, Jan. 1991.

[135] G. Lazzi and O. P. Gandhi, "A mixed fdtd-integral equation approach for on-site safety assessment in complex electromagnetic environments," *IEEE Trans. Antennas Propag.*, vol. 48, no. 12, pp. 1830–1836, Dec. 2000.

[136] M. A. Jensen and Y. Rahmat-Samii, "EM interaction of handset antennas and a human in personal communications," *Proc. IEEE*, vol. 83, no. 1, pp. 7–17, Jan. 1995.

[137] C. M. Furse, J.-Y. Chen, and O. P. Gandhi, "The use of the frequency-dependent finite-difference time-domain method for induced current and SAR calculations for a heterogeneous model of the human body," *IEEE Trans. Electromagn. Compat.*, vol. 36, no. 2, pp. 128–133, May 1994.

[138] P. Dimbylow and S. Mann, "SAR calculations in an anatomically realistic model of the head for mobile communication transceivers at 900 MHz and 1.8 GHz," *Phys. Med. Biol.*, vol. 39, no. 10, p. 1537, 1994.

[139] K. Fujii, K. Ito, and S. Tajima, "A study on the receiving signal level in relation with the location of electrodes for wearable devices using human body as a transmission channel," in *Proc. IEEE Antennas Propag. Soc. Int. Symp.*, vol. 3, 2003, pp. 1071–1074.

[140] K. Fujii and K. Ito, "Evaluation of the received signal level in relation to the size and carrier frequencies of the wearable device using human body as a transmission channel," in *Proc. IEEE Antennas Propag. Soc. Symp.*, vol. 1, 2004, pp. 105–108.

[141] K. Ito, M. Takahashi, and K. Fujii, *Transmission Mechanism of Wearable Devices Using the Human Body as a Transmission Channel*. London, U.K.: Artech House, 2006, pp. 65–92.

[142] K. Fujii, M. Takahashi, and K. Ito, "Electric field distributions of wearable devices using the human body as a transmission channel," *IEEE Trans. Antennas Propag.*, vol. 55, no. 7, pp. 2080–2087, Jul. 2007.

[143] J. Wang, Y. Nishikawa, and T. Shibata, "Analysis of on-body transmission mechanism and characteristic based on an electromagnetic field approach," *IEEE Trans. Microw. Theory Techn.*, vol. 57, no. 10, pp. 2464–2470, Oct. 2009.

[144] R. A. Receveur *et al.*, "Microsystem technologies for implantable applications," *J. Micromech. Microeng.*, vol. 17, no. 5, p. R50, 2007.

[145] K. Y. Yazdandoos and K. Sayrafian-Pour, *Channel Model for Body Area Network (BAN)*, IEEE Standard P802.15-08-0780-12-0006, Nov. 2010.

[146] K. Sayrafian, *MICS Channel Characteristics, Preliminary Results*, IEEE Standard 802.15-08-0351-00-0006, May 2008.

[147] K. Sayrafian, *A Statistical Path Loss Model for MICS*, IEEE Standard 802.15-08-0519-01-0006 Sep. 2008.

[148] C. Garcia-Pardo *et al.*, "Ultrawideband technology for medical in-body sensor networks: An overview of the human body as a propagation medium, phantoms, and approaches for propagation analysis," *IEEE Antennas Propag. Mag.*, vol. 60, no. 3, pp. 19–33, Jun. 2018.

[149] A. Alomainy and Y. Hao, "Modeling and characterization of biotelemetric radio channel from ingested implants considering organ contents," *IEEE Trans. Antennas Propag.*, vol. 57, no. 4, pp. 999–1005, Apr. 2009.

[150] B. Zhen, K. Takizawa, T. Aoyagi, and R. Kohno, "A body surface coordinator for implanted biosensor networks," in *Proc. IEEE ICC*, 2009, pp. 1–5.

[151] R. Chávez-Santiago *et al.*, "Experimental path loss models for in-body communications within 2.36–2.5 GHz," *IEEE J. Biomed. Health Inform.*, vol. 19, no. 3, pp. 930–937, May 2015.

[152] A. Khaleghi, R. Chávez-Santiago, and I. Balasingham, "Ultra-wideband statistical propagation channel model for implant sensors in the human chest," *IET Microw. Antennas Propag.*, vol. 5, no. 15, pp. 1805–1812, 2011.

[153] K. M. S. Thotahewa, J. Redouté, and M. R. Yuce, "Propagation Power absorption, and temperature analysis of UWB wireless capsule endoscopy devices operating in the human body," *IEEE Trans. Microw. Theory Techn.*, vol. 63, no. 11, pp. 3823–3833, Nov. 2015.

[154] Y. Shimizu, T. Furukawa, D. Anzai, and J. Wang, "Performance improvement by transmit diversity technique for implant ultra-wideband communication," *IET Microw. Antennas Propag.*, vol. 10, no. 10, pp. 1106–1112, 2016.

[155] J. Shi and J. Wang, "Channel characterization and diversity feasibility for in-body to on-body communication using low-band UWB signals," in *Proc. Int. Symp. Appl. Sci. Biomed. Commun. Technol.*, 2010, pp. 1–4.

[156] M. Kanaan and M. Suveren, "A novel frequency-dependent path loss model for ultra wideband implant body area networks," *Measurement*, vol. 68, pp. 117–127, May 2015.

[157] P. S. Hall, M. Ricci, and T. M. Hee, "Measurements of on-body propagation characteristics," in *Proc. IEEE Antennas Propag. Soc. Int. Symp.*, vol. 2, 2002, pp. 310–313.

[158] T. Aoyagi *et al.*, *Channel Model for Wearable and Implantable WBANs*, IEEE Standard 802.15-08-0416-04-0006, Nov. 2008.

[159] G. Dolmans and A. Fort, *Channel Models WBAN-Holst Centre/IMEC-NL*, IEEE Standard 802.15-08-0418-01-0006, Jul. 2008.

[160] E. Reusens *et al.*, "Characterization of on-body communication channel and energy efficient topology design for wireless body area networks," *IEEE Trans. Inf. Technol. Biomed.*, vol. 13, no. 6, pp. 933–945, Nov. 2009.

[161] A. Fort *et al.*, "Indoor body-area channel model for narrowband communications," *IET Microw. Antennas Propag.*, vol. 1, no. 6, pp. 1197–1203, Dec. 2007.

[162] A. Fort, C. Desset, J. Ryckaert, P. De Doncker, L. van Biesen, and P. Wambacq "Characterization of the ultra wideband body area propagation channel," in *Proc. IEEE Int. Conf. UWB*, Sep. 2005, p. 6.

[163] Y. Chen *et al.*, "Cooperative communications in ultra-wideband wireless body area networks: Channel modeling and system diversity analysis," *IEEE J. Sel. Areas Commun.*, vol. 27, no. 1, pp. 5–16, Jan. 2009.

[164] S. van Roy *et al.*, "Dynamic channel modeling for multi-sensor body area networks," *IEEE Trans. Antennas Propag.*, vol. 61, no. 4, pp. 2200–2208, Apr. 2013.

[165] A. Sani *et al.*, "Experimental characterization of UWB on-body radio channel in indoor environment considering different antennas," *IEEE Trans. Antennas Propag.*, vol. 58, no. 1, pp. 238–241, Jan. 2010.

[166] T. Kumpuniemi, T. Tuovinen, M. Hämäläinen, K. Y. Yazdandoost, R. Vuohtoniemi, and J. Iinatti, "Measurement-based on-body path loss modelling for UWB wBAN communications," in *Proc. Int. Symp. Med. Inf. Commun. Technol.*, 2013, pp. 233–237.

[167] A. Fort, C. Desset, P. De Doncker, P. Wambacq, and L. Van Biesen, "An ultra-wideband body area propagation channel model-from statistics to

implementation," *IEEE Trans. Microw. Theory Techn.*, vol. 54, no. 4, pp. 1820–1826, Jun. 2006.
[168] Y. P. Zhang and Q. Li, "Performance of UWB impulse radio with planar monopoles over on-human-body propagation channel for wireless body area networks," *IEEE Trans. Antennas Propag.*, vol. 55, no. 10, pp. 2907–2914, Oct. 2007.
[169] A. Fort, J. Ryckaert, C. Desset, P. De Doncker, P. Wambacq, and L. Van Biesen, "Ultra-wideband channel model for communication around the human body," *IEEE J. Sel. Areas Commun.*, vol. 24, no. 4, pp. 927–933, Apr. 2006.
[170] P. Thirumaraiselvan, K. S. Sankaran, V. B. Geo, V. R. Prakash, and N. Vasudevan, "A statistical lower UWB channel model for in body communications," *Mobile Netw. Appl.*, vol. 24, no. 6, pp. 1814–1820, 2019.
[171] M. Mackowiak and L. M. Correia, "Statistical path loss model for dynamic off-body channels," in *Proc. IEEE PIMRC*, 2014, pp. 53–57.
[172] A. F. Molisch *et al.*, "A comprehensive model for ultrawideband propagation channels," in *Proc. IEEE GLOBECOM*, 2005, p. 3653.
[173] R. Rosini and R. D'Errico, "Off-body channel modelling at 2.45 GHz for two different antennas," in *Proc. Eur. Conf. Antennas Propag.*, 2012, pp. 3378–3382.
[174] M. Särestöniemi, T. Tuovinen, M. Hämäläinen, K. Y. Yazdandoost, and J. Iinatti, "Channel modeling for UWB wBAN on-off body communication link with finite integration technique," in *Proc. BODYNETS*, 2012, pp. 235–241.
[175] D. B. Smith *et al.*, "First- and second-order statistical characterizations of the dynamic body area propagation channel of various bandwidths," *Ann. Telecommun.*, vol. 66, no. 3, pp. 187–203, 2011.
[176] T. Zasowski, F. Althaus, M. Stager, A. Wittneben, and G. Troster, "UWB for noninvasive wireless body area networks: Channel measurements and results," in *Proc. IEEE Conf. Ultra Wideband Syst. Technol.*, Nov. 2003, pp. 285–289.
[177] Y. I. Nechayev, P. S. Hall, I. Khan, and C. C. Constantinou, "Wireless channels and antennas for body-area networks," in *Proc. Int. Conf. Wireless On-Demand Netw. Syst. Services*, 2010, pp. 137–144.
[178] D. B. Smith, D. Miniutti, L. W. Hanlen, D. Rodda, and B. Gilbert, "Dynamic narrowband body area communications: Link-margin based performance analysis and second-order temporal statistics," in *Proc. IEEE WCNC*, 2010, pp. 1–6.
[179] D. B. Smith, T. Lamahewa, L. W. Hanlen, and D. Miniutti, "Simple prediction-based power control for the on-body area communications channel," in *Proc. IEEE ICC*, 2011, pp. 1–5.
[180] P. Sroka and J. A. Samuels, "Adaptive antenna matching," U.S. Patent 5 778 308, Jul. 7, 1998.
[181] P. W. Dent and R. A. Dolman, "System and method for adaptive antenna impedance matching," U.S. Patent 6 845 126, Jan. 18, 2005.
[182] P. W. Dent and S. Mattisson, "System and method for adaptive antenna impedance matching," U.S. Patent 8 351 874, Jan. 8, 2013.
[183] C. Roblin *et al.*, "Antenna design and channel modeling in the BAN context—Part I: Antennas," *Ann. Telecommun.*, vol. 66, nos. 3–4, pp. 139–155, 2011.
[184] S. Yan, P. J. Soh, and G. A. E. Vandenbosch, "Wearable ultrawideband technology—A review of ultrawideband antennas, propagation channels, and applications in wireless body area networks," *IEEE Access*, vol. 6, pp. 42177–42185, 2018.
[185] T. G. Zimmerman, "Personal area networks: Near-field intrabody communication," *IBM Syst. J.*, vol. 35, nos. 3–4, pp. 609–617, 1996.
[186] T. Handa, S. Shoji, S. Ike, S. Takeda, and T. Sekiguchi, "A very low-power consumption wireless ECG monitoring system using body as a signal transmission medium," in *Proc. Int. Solid-State Sensors Actuators Conf.*, vol. 2, 1997, pp. 1003–1006.
[187] T. Ogasawara, A.-I. Sasaki, K. Fujii, and H. Morimura, "Human body communication based on magnetic coupling," *IEEE Trans. Antennas Propag.*, vol. 62, no. 2, pp. 804–813, Feb. 2014.
[188] M. S. Wegmueller, M. Oberle, N. Felber, N. Kuster, and W. Fichtner, "Signal transmission by galvanic coupling through the human body," *IEEE Trans. Instrum. Meas.*, vol. 59, no. 4, pp. 963–969, Apr. 2010.
[189] J. Bae *et al.*, "The signal transmission mechanism on the surface of human body for body channel communication," *IEEE Trans. Microw. Theory Techn.*, vol. 60, no. 3, pp. 582–593, Mar. 2012.
[190] A. K. Teshome, B. Kibret, and D. T. H. Lai, "Galvanically coupled intrabody communications for medical implants: A unified analytic model," *IEEE Trans. Antennas Propag.*, vol. 64, no. 7, pp. 2989–3002, Jul. 2016.
[191] N. Cho, J. Yoo, S.-J. Song, J. Lee, S. Jeon, and H.-J. Yoo, "The human body characteristics as a signal transmission medium for intrabody communication," *IEEE Trans. Microw. Theory Techn.*, vol. 55, no. 5, pp. 1080–1086, May 2007.
[192] Y. Song, Q. Hao, K. Zhang, M. Wang, Y. Chu, and B. Kang, "The simulation method of the galvanic coupling intrabody communication with different signal transmission paths," *IEEE Trans. Instrum. Meas.*, vol. 60, no. 4, pp. 1257–1266, Apr. 2011.
[193] M. A. Callejón, D. Naranjo-Hernandez, J. Reina-Tosina, and L. M. Roa, "Distributed circuit modeling of galvanic and capacitive coupling for intrabody communication," *IEEE Trans. Biomed. Eng.*, vol. 59, no. 11, pp. 3263–3269, Nov. 2012.
[194] B. Kibret, M. Seyedi, D. T. H. Lai, and M. Faulkner, "Investigation of galvanic-coupled intrabody communication using the human body circuit model," *IEEE J. Biomed. Health Informat.*, vol. 18, no. 4, pp. 1196–1206, Jul. 2014.
[195] M. Pereira, G. Alvarez, and F. de Sousa, "Modeling of the test fixtures to improve the hbc channel interpretation," in *Proc. IEEE I2MTC*, 2015, pp. 1753–1756.
[196] M. D. Pereira, G. A. Alvarez-Botero, and F. R. de Sousa, "Characterization and modeling of the capacitive hbc channel," *IEEE Trans. Instrum. Meas.*, vol. 64, no. 10, pp. 2626–2635, Oct. 2015.
[197] M. Swaminathan, F. S. Cabrera, J. S. Pujol, U. Muncuk, G. Schirner, and K. R. Chowdhury, "Multi-path model and sensitivity analysis for galvanic coupled intra-body communication through layered tissue," *IEEE Trans. Biomed. Syst.*, vol. 10, no. 2, pp. 339–351, Apr. 2016.
[198] J. Mao, H. Yang, Y. Lian, and B. Zhao, "A five-tissue-layer human body communication circuit model tunable to individual characteristics," *IEEE Trans. Biomed. Circuits Syst.*, vol. 12, no. 2, pp. 303–312, Apr. 2018.
[199] S. Maity, M. He, M. Nath, D. Das, B. Chatterjee, and S. Sen, "Bio-physical modeling, characterization, and optimization of electro-quasistatic human body communication," *IEEE Trans. Biomed. Eng.*, vol. 66, no. 6, pp. 1791–1802, Jun. 2019.
[200] I. N. Alquaydheb, A. E. Khorshid, and A. M. Eltawil, "Analysis and estimation of intra-body communications path loss for galvanic coupling," *Advances in Body Area Networks I*, G. Fortino and Z. Wang, Eds. Cham, Switzerland: Springer Int., 2019, pp. 267–277.
[201] J. Park, H. Garudadri, and P. P. Mercier, "Channel modeling of miniaturized battery-powered capacitive human body communication systems," *IEEE Trans. Biomed. Eng.*, vol. 64, no. 2, pp. 452–462, Feb. 2017.
[202] Ž. Lucev, I. Krois, and M. Cifrek, "A capacitive intrabody communication channel from 100 KHz to 100 MHz," *IEEE Trans. Instrum. Meas.*, vol. 61, no. 12, pp. 3280–3289, Dec. 2012.
[203] J.-H. Hwang, T.-W. Kang, Y.-T. Kim, and S.-O. Park, "Measurement of transmission properties of HBC channel and its impulse response model," *IEEE Trans. Instrum. Meas.*, vol. 65, no. 1, pp. 177–188, Jan. 2016.
[204] Y. Liu, J. Kuang, Z. He, and J. Fang, "Measurement system for propagation characteristics of intra-body communication," in *Proc. IEEE Int. Conf. Wireless Commun. Netw. Mobile Comput.*, 2010, pp. 1–4.
[205] J. A. Ruiz and S. Shimamoto, "Experimental evaluation of body channel response and digital modulation schemes for intra-body communications," in *Proc. IEEE ICC*, vol. 1, 2006, pp. 349–354.
[206] J. A. Ruiz, J. Xu, and S. Shimamoto, "Propagtion characteristics of intra-body communications for body area networks," in *Proc. IEEE Consum. Commun. Netw. Conf.*, vol. 1, 2006, pp. 509–513.
[207] R. Xu, H. Zhu, and J. Yuan, "Characterization and analysis of intra-body communication channel," in *Proc. IEEE Antennas Propag. Soc. Int. Symp.*, 2009, pp. 1–4.
[208] W.-C. Wang, Z.-D. Nie, F. Guan, T. Leng, and L. Wang, "Experimental studies on human body communication characteristics based upon capacitive coupling," in *Proc. IEEE Int. Conf. Body Sensor Netw.*, 2011, pp. 180–185.
[209] T. C. W. Schenk, N. S. Mazloum, L. Tan, and P. Rutten, "Experimental characterization of the body-coupled communications channel," in *Proc. IEEE Int. Symp. Wireless Commun. Syst.*, 2008, pp. 234–239.
[210] N. Zedong, M. Jingjing, K. Ivanov, and W. Lei, "An investigation on dynamic human body communication channel characteristics at 45 MHz in different surrounding environments," *IEEE Antennas Wireless Propag. Lett.*, vol. 13, pp. 309–312, 2014.
[211] M. A. Callejón, J. Reina-Tosina, D. Naranjo-Hernández, and L. M. Roa, "Measurement issues in galvanic intrabody communication: Influence of experimental setup," *IEEE Trans. Biomed. Eng.*, vol. 62, no. 11, pp. 2724–2732, Nov. 2015.
[212] G. A. Álvarez-Botero, Y. K. Hernández-Gómez, C. E. Telléz, and J. F. Coronel, "Human body communication: Channel characterization issues," *IEEE Instrum. Meas. Mag.*, vol. 22, no. 5, pp. 48–53, Oct. 2019.

[213] M. A. Callejón, D. Naranjo-Hernández, J. Reina-Tosina, and L. M. Roa, "A comprehensive study into intrabody communication measurements," *IEEE Trans. Instrum. Meas.*, vol. 62, no. 9, pp. 2446–2455, Sep. 2013.
[214] S. Schwingenschuh *et al.*, "Assessment of skin permeability to topically applied drugs by skin impedance and admittance," *Physiol. Meas.*, vol. 38, no. 11, p. N138, 2017.
[215] F. Lu *et al.*, "Review of stratum corneum impedance measurement in non-invasive penetration application," *Biosensors*, vol. 8, no. 2, p. 31, 2018.
[216] Y. Meng, Z. Li, and J. Chen, "A flexible dry electrode based on APTES-anchored PDMs substrate for portable ECG acquisition system," *Microsyst. Technol.*, vol. 22, no. 8, pp. 2027–2034, 2016.
[217] A. J. Bandodkar, W. Jia, C. Yardimci, X. Wang, J. Ramirez, and J. Wang, "Tattoo-based noninvasive glucose monitoring: A proof-of-concept study," *Anal. Chem.*, vol. 87, no. 1, pp. 394–398, 2015.
[218] Y. Chen *et al.*, "Skin-like biosensor system via electrochemical channels for noninvasive blood glucose monitoring," *Sci. Adv.*, vol. 3, no. 12, 2017, Art. no. e1701629.
[219] S. Yao and Y. Zhu, "Nanomaterial-enabled dry electrodes for electrophysiological sensing: A review," *J. Mineral. Metals Mater. Soc.*, vol. 68, pp. 1145–1155, 2016. [Online]. Available: https://link.springer.com/article/10.1007%2Fs11837-016-1818-0#citeas
[220] S. Yao and Y. Zhu, "Nanomaterial-enabled dry electrodes for electrophysiological sensing: A review," *J. Manag.*, vol. 68, no. 4, pp. 1145–1155, 2016.
[221] C.-U. Kim *et al.*, "Numerical analysis on effective electric field penetration depth for interdigital impedance sensor," *J. Phys. Conf.*, vol. 418, no. 1, 2013, Art. no. 012020.
[222] M. Varshney and Y. Li, "Interdigitated array microelectrodes based impedance biosensors for detection of bacterial cells," *Biosensors Bioelectron.*, vol. 24, no. 10, pp. 2951–2960, 2009.
[223] B. Zhao, J. Mao, J. Zhao, H. Yang, and Y. Lian, "The role and challenges of body channel communication in wearable flexible electronics," *IEEE Trans. Biomed. Circuits Syst.*, vol. 14, no. 2, pp. 283–296, Apr. 2020.
[224] H. Wang, X. Tang, C. S. Choy, and G. E. Sobelman, "Cascaded network body channel model for intrabody communication," *IEEE J. Biomed. Health Inform.*, vol. 20, no. 4, pp. 1044–1052, Jul. 2016.
[225] B. Zhao, Y. Lian, A. M. Niknejad, and C. H. Heng, "A low-power compact IEEE 802.15.6 compatible human body communication transceiver with digital Sigma–Delta IIR mask shaping," *IEEE J. Solid-State Circuits*, vol. 54, no. 2, pp. 346–357, Feb. 2019.
[226] J. Bae, K. Song, H. Lee, H. Cho, and H.-J. Yoo, "A 0.24-nj/b wireless body-area-network transceiver with scalable double-FSK modulation," *IEEE J. Solid-State Circuits*, vol. 47, no. 1, pp. 310–322, Jan. 2012.
[227] Y. L. Tsou, C.-S. A. Gong, N. C. Cheng, Y. Lee, and C. F. Jou, "Integrated biosensing platform based on a 1.74-mw- 90-dbm sensitivity dual-mode-operation receiver for IEEE 802.15.6 human body communication standard," *IEEE Sensors J.*, vol. 15, no. 6, pp. 3317–3327, Jun. 2014.
[228] K.-R. Lee, J. Jang, H. Cho, and H.-J. Yoo, "A 635 μw non-contact compensation IC for body channel communication," in *Proc. IEEE ISCAS*, 2016, pp. 1406–1409.
[229] J. Zhao, J. Mao, T. Zhou, L. Lai, H. Yang, and B. Zhao, "An auto loss compensation system for non-contact capacitive coupled body channel communication," in *Proc. IEEE ISCAS*, 2018, pp. 1–5.
[230] Y. Liu, Z. Tan, H. Hu, L. J. Cimini, and G. Y. Li, "Channel estimation for OFDM," *IEEE Commun. Surveys Tuts.*, vol. 16, no. 4, pp. 1891–1908, 4th Quart., s2014.
[231] M. Morelli and U. Mengali, "A comparison of pilot-aided channel estimation methods for OFDM systems," *IEEE Trans. Signal Process.*, vol. 49, no. 12, pp. 3065–3073, Dec. 2001.
[232] M. C. Valenti and B. D. Woerner, "Iterative channel estimation and decoding of pilot symbol assisted turbo codes over flat-fading channels," *IEEE J. Sel. Areas Commun.*, vol. 19, no. 9, pp. 1697–1705, Sep. 2001.
[233] H. Ye, G. Y. Li, and B. Juang, "Power of deep learning for channel estimation and signal detection in OFDM systems," *IEEE Wireless Commun. Lett.*, vol. 7, no. 1, pp. 114–117, Feb. 2018.
[234] H. Huang, J. Yang, H. Huang, Y. Song, and G. Gui, "Deep learning for super-resolution channel estimation and DOA estimation based massive MIMO system," *IEEE Trans. Veh. Technol.*, vol. 67, no. 9, pp. 8549–8560, Sep. 2018.
[235] X. Lin, N. B. Shroff, and R. Srikant, "A tutorial on cross-layer optimization in wireless networks," *IEEE J. Sel. Areas Commun.*, vol. 24, no. 8, pp. 1452–1463, Aug. 2006.
[236] H. Yetgin, K. T. K. Cheung, M. El-Hajjar, and L. H. Hanzo, "A survey of network lifetime maximization techniques in wireless sensor networks," *IEEE Commun. Surveys Tuts.*, vol. 19, no. 2, pp. 828–854, 2nd Quart., 2017.
[237] T. Wu, T. S. Rappaport, and C. M. Collins, "The human body and millimeter-wave wireless communication systems: Interactions and implications," in *Proc. IEEE ICC*, 2015, pp. 2423–2429.
[238] M. Li, W. Lou, and K. Ren, "Data security and privacy in wireless body area networks," *IEEE Wireless Commun.*, vol. 17, no. 1, pp. 51–58, Feb. 2010.
[239] D. Das, S. Maity, B. Chatterjee, and S. Sen, "Enabling covert body area network using electro-quasistatic human body communication," *Sci. Rep.*, vol. 9, no. 1, pp. 1–14, 2019.

Abdulkadir Celik (Senior Member, IEEE) received the first M.S. degree in electrical engineering, the second M.S. degree in computer engineering, and the Ph.D. degree in co-majors of electrical engineering and computer engineering from Iowa State University, Ames, IA, USA, in 2013, 2015, and 2016, respectively.

He was a Postdoctoral Fellow with the King Abdullah University of Science and Technology, Thuwal, Saudi Arabia, from 2016 to 2020, where he has been a Research Scientist with the Communications and Computing Systems Lab since 2020. His research interests are in the areas of wireless communication systems and networks.

Khaled N. Salama (Senior Member, IEEE) received the B.S. degree from the Department of Electronics and Communications, Cairo University, Cairo, Egypt, in 1997, and the M.S. and Ph.D. degrees from the Department of Electrical Engineering, Stanford University, Stanford, CA, USA, in 2000 and 2005, respectively.

He was an Assistant Professor with the Rensselaer Polytechnic Institute, Troy, NY, USA, from 2005 to 2009. In 2009, he joined the King Abdullah University of Science and Technology (KAUST), Thuwal, Saudi Arabia, where he is currently a Professor, and he was the Founding Program Chair until 2011. He is the Director of Sensors Initiative, a consortium of nine universities, including KAUST; Massachusetts Institute of Technology, Cambridge, MA, USA; the University of California at Los Angeles, Los Angeles, CA, USA; the Georgia Institute of Technology, Atlanta, GA, USA; Brown University, Providence, RI, USA; Delft University of Technology, Delft, The Netherlands; Swansea University, Swansea, U.K.; the University of Regensburg, Regensburg, Germany; and the Australian Institute of Marine Science, Townsville, QLD, Australia. He has authored 250 articles and 20 issued U.S. patents on low-power mixed-signal circuits for intelligent fully integrated sensors and neuromorphic circuits using memristor devices.

Dr. Salama's work on CMOS sensors for molecular detection has been funded by the National Institutes of Health and the Defense Advanced Research Projects Agency, awarded the Stanford-Berkeley Innovators Challenge Award in biological sciences and was acquired by Lumina Inc.

Ahmed M. Eltawil (Senior Member, IEEE) received the M.Sc. and B.Sc. degrees (Hons.) from Cairo University, Giza, Egypt, in 1999 and 1997, respectively, and the Ph.D. degree from the University of California at Los Angeles, Los Angeles, CA, USA, in 2003.

Since 2019, he has been a Professor with the Computer, Electrical and Mathematical Science and Engineering Division, King Abdullah University of Science and Technology, Thuwal, Saudi Arabia. Since 2005, he has been with the Department of Electrical Engineering and Computer Science, University of California at Irvine, Irvine, CA, USA, where he founded the Wireless Systems and Circuits Laboratory. His research interests are in the general area of low power digital circuit and signal processing architectures with an emphasis on mobile systems.

Dr. Eltawil received several awards, as well as distinguished grants, including the NSF CAREER Grant supporting his research in low power systems. He has been on the technical program committees and steering committees for numerous workshops, symposia, and conferences in the areas of low power computing and wireless communication system design.